Metals in the $z \sim 3$ intergalactic medium: results from an ultra-high signal-to-noise ratio UVES quasar spectrum

V. D'Odorico,[1]★ S. Cristiani,[1,2]★ E. Pomante,[1] R. F. Carswell,[3] M. Viel,[1,2] P. Barai,[1,4]
G. D. Becker,[5] F. Calura,[6] G. Cupani,[1] F. Fontanot,[1] M. G. Haehnelt,[3,7] T-S. Kim,[1]
J. Miralda-Escudé,[8,9] A. Rorai,[3,7] E. Tescari[10,11] and E. Vanzella[6]

[1]*INAF – Osservatorio Astronomico di Trieste, Via Tiepolo 11, I-34143 Trieste, Italy*
[2]*INFN/National Institute of Nuclear Physics, via Valerio 2, I-34127 Trieste, Italy*
[3]*Institute of Astronomy, Madingley Road, Cambridge CB3 0HA, UK*
[4]*Scuola Normale Superiore di Pisa, Piazza dei Cavalieri 7, I-56126 Pisa, Italy*
[5]*Department of Physics and Astronomy, University of California, Riverside, CA 92521, USA*
[6]*INAF – Osservatorio Astronomico di Bologna, Via Ranzani 1, I-40127 Bologna, Italy*
[7]*Kavli Institute of Cosmology, Madingley Road, Cambridge CB3 0HA, UK*
[8]*Institució Catalana de Recerca i Estudis Avançats, Passeig de Lluís Companys, 23, E-08010 Barcelona, Catalonia, Spain*
[9]*Institut de Ciències del Cosmos, Universitat de Barcelona, ICC-UB, Martí i Franquès, 1, Barcelona E-08028, Catalonia, Spain*
[10]*School of Physics, The University of Melbourne, Parkville VIC 3010, Australia*
[11]*ARC Centre of Excellence for All-sky Astrophysics (CAASTRO)*

ABSTRACT

In this work, we investigate the abundance and distribution of metals in the intergalactic medium (IGM) at $\langle z \rangle \simeq 2.8$ through the analysis of an ultra-high signal-to-noise ratio UVES spectrum of the quasar HE0940-1050. In the C IV forest, our deep spectrum is sensitive at 3σ to lines with column density down to $\log N_{\rm CIV} \simeq 11.4$ and in 60 per cent of the considered redshift range down to $\simeq 11.1$. In our sample, all H I lines with $\log N_{\rm HI} \geq 14.8$ show an associated C IV absorption. In the range $14.0 \leq \log N_{\rm HI} < 14.8$, 43 per cent of H I lines has an associated C IV absorption. At $\log N_{\rm HI} < 14.0$, the detection rates drop to <10 per cent, possibly due to our sensitivity limits and not to an actual variation of the gas abundance properties. In the range $\log N_{\rm HI} \geq 14$, we observe a fraction of H I lines with detected C IV a factor of 2 larger than the fraction of H I lines lying in the circumgalactic medium (CGM) of relatively bright Lyman-break galaxies hosted by dark matter haloes with $\langle M \rangle \sim 10^{12}$ M$_\odot$. The comparison of our results with the output of a grid of photoionization models and of two cosmological simulations implies that the volume filling factor of the IGM gas enriched to a metallicity $\log Z/Z_\odot \gtrsim -3$ should be of the order of $\sim$10–13 per cent. In conclusion, our results favour a scenario in which metals are found also outside the CGM of bright star-forming galaxies, possibly due to pollution by lower mass objects and/or to an early enrichment by the first sources.

Key words: galaxies: abundances – intergalactic medium – quasars: absorption lines – cosmology: observations.

1 INTRODUCTION

The observed properties and evolution of galaxies in the Universe require the existence of mechanisms regulating and quenching star formation. Models and simulations which are not implementing these *feedback* processes predict e.g. galaxies with far larger stellar masses than are observed (e.g. Katz, Weinberg & Hernquist 1996; Somerville & Primack 1999; Cole et al. 2000; Springel & Hernquist

2003; Kereš et al. 2009, and references therein). Stellar winds, the explosion of supernovae and winds from active galactic nuclei (AGN) all contribute to the heating and expulsion of gas from the disc and the bulge of galaxies into the halo and possibly far away into the lower density gas. The signatures of strong winds are widely observed in local star forming galaxies (see e.g. Veilleux, Cecil & Bland-Hawthorn 2005, for a review). Their presence at high redshift has been probed spectroscopically by the observed offsets between the redshifts of the nebular emission lines and those of the interstellar absorption lines in spectra of lensed or extremely bright Lyman-break galaxies (LBGs, e.g. Pettini et al. 2001; Shapley et al.

★ E-mail: dodorico@oats.inaf.it (VD'O); cristiani@oats.inaf.it (SC)

2003; Martin 2005; Rupke, Veilleux & Sanders 2005; Tremonti, Moustakas & Diamond-Stanic 2007; Weiner et al. 2009) and has been explored in cosmological hydrodynamical simulations (e.g. Tescari et al. 2011; Barai et al. 2013). Recently, direct observational evidence for powerful, quasar-driven outflows has emerged (e.g. Feruglio et al. 2010; Rupke & Veilleux 2011; Sturm et al. 2011; Greene, Zakamska & Smith 2012; Maiolino et al. 2012; Cicone et al. 2014; Harrison et al. 2014). These outflows extend over scales of several kpc from the nucleus and have been detected in both atomic and molecular gas.

The indisputable evidence of the existence of galactic outflows leaves open one fundamental question: how far is this gas travelling? Most of the times, the measured outflowing velocities are large enough to allow the escape of the gas from the virial radius (e.g. Pettini et al. 2001; Vanzella et al. 2010) and theoretical models predict that the expanding material may reach characteristic distances of a few hundred kpc and up to ∼1 Mpc (e.g. Aguirre et al. 2001; Calura & Matteucci 2006; Samui et al. 2008).

The presence of products of the stellar nucleosynthesis outside galaxies has been confirmed by the first high-resolution, high signal-to-noise ratio (SNR) optical spectra of high redshift quasars used as background bright sources. In those spectra, weak absorption features mainly due to the ionic doublet of C IV at $z_{abs} \sim$ 2–3 (log $N_{CIV} \geq$ 12) were detected at the same redshift of about half of the H I Lyman α (Lyα) lines with column density log $N_{HI} \geq$ 14.5 and of all Lyα lines with log $N_{HI} \geq$ 15 (Tytler et al. 1995; Cowie et al. 1995; Songaila & Cowie 1996). In the same years, thanks to theoretical models and hydrodynamical simulations, the so called Lyα forest of H I lines, observed in the spectra of high-redshift quasars, was interpreted as due mainly to the density fluctuations in the diffuse gas between galaxies: the intergalactic medium (IGM, see e.g. Cen et al. 1994; Petitjean, Mueket & Kates 1995; or Rauch 1998; Weinberg et al. 1999, for reviews).

The presence of heavy elements in gas outside the virial radius of galaxies confirmed observationally the effectiveness of outflows and generated a new question: have the metals, that we observe associated with the Lyα forest at $z \sim$ 2–3, been ejected by the co-eval population of star forming galaxies or are they due (also) to previous generations of galaxies?

Indeed, models of the H I re-ionization process foresee that the same sources which re-ionized the Universe were also able to pollute the gas to a metallicity floor of the order log (Z/Z$_\odot$) $\simeq$ −3 (e.g. Madau, Ferrara & Rees 2001). The volume filling factor of the metals due to this pre-enrichment depends on the nature of the sources, with the star-forming haloes with the smallest masses being the most efficient pollutant of the IGM on large scales (e.g. Bertone, Stoehr & White 2005).

To test observationally this scenario, efforts have been concentrated on two main approaches: the detection of metals in the outskirts of galaxies and the investigation of the level of pollution in the low density gas at overdensities of a few.

Metals close to galaxies are generally searched for considering the correlation between the metal absorptions observed along a quasar line of sight and the galaxies at matching redshifts present in the field. All the studies carried out up to now both at high (e.g. Adelberger et al. 2005; Steidel et al. 2010; Turner et al. 2014) and low redshift (e.g. Prochaska et al. 2011; Tumlinson et al. 2011; Werk et al 2013; Bordoloi et al. 2014; Liang & Chen 2014) agree on the significant presence of metals in high and low ionization state at impact parameters at least as large as ≈100–300 kpc. However, this piece of evidence is not sufficient to state that the observed metals were freshly ejected by the associated galaxies, since the

same correlation at $z \sim$ 2–3 could originate from the accumulation of older metals in the knots of the cosmic web due to gravitational collapse (e.g. Porciani & Madau 2005). Similar results for the size of the regions enriched by galaxies were found based on the clustering properties of metal absorbers (mainly C IV lines) along (e.g. Scannapieco et al. 2006) and across (e.g. Martin et al. 2010) the lines of sight to distant quasars.

A few years after the discovery of the first metals polluting the IGM, the exploration of the low density regime was attempted using the stacking method (Lu et al. 1998) and the individual pixel optical depths (POD) of Lyα and C IV (Cowie & Songaila 1998). However, rigorous testing of the analysis procedures by Ellison et al. (1999) revealed that in particular the stacking method suffered from severe limitations, leaving the question of whether or not the low density regions of the IGM were enriched unanswered.

The next step to reach the metallicity level due to a possible pre-enrichment was the observation of an exceptionally high SNR spectrum of the gravitationally lensed quasar B1422+231 (z_{em} = 3.623) with the high resolution spectrograph HIRES at the Keck telescope. Ellison et al. (2000, ESSP00 hereafter) showed that the 5σ detection limit for C IV outside the Lyα forest in this object is log $N_{CIV} \simeq$ 11.6 for a Doppler value b = 13 km s^{-1} and the column density distribution function corrected for completeness is fitted by the same power law at least down to log N_{CIV} = 11.75, without showing a downturn. The POD result is consistent with an almost constant log (C IV/H I) $\sim$ −2.6 down to τ(Lyα) $\sim$ 2–3 which implies a contribution of C IV absorbers with column densities below the detection limit.

Further studies based on the POD technique have been carried out with larger samples (Schaye et al. 2003; Aracil et al. 2004). In particular, Schaye et al. (2003, S03 hereafter) based their study on the high SNR spectrum of B1422+231 plus other 18 objects observed at lower SNR. They used hydrodynamical simulations to convert the measurement of the relation between the optical depths τ_{CIV} and τ_{HI} into a relation between [C/H], overdensity[1] and redshift. They found that for a fixed overdensity and redshift, the metallicity distribution is close to lognormal with a large scatter (e.g. σ([C/H]) $\simeq$0.7 at δ = 5 and z = 3); the median metallicity does not vary significantly with redshift in the range z = 1.8–4.1, while it decreases with the overdensity:

$$[C/H] \simeq -3.47 + 0.65(\log \delta - 0.5) + 0.08(z - 3) \tag{1}$$

and the relation is valid down to approximately the mean density. This result, due to its statistical nature, lacks the information on the distribution and covering factor of metals which could only be derived by a direct detection of the very weak metal lines and their association with the corresponding Lyα lines.

After the pioneer work by ESSP00, the most ambitious surveys for weak associated metal absorption features (based on Voigt profile fitting of C IV lines) have detected C IV with log N_{CIV}>12 associated with H I absorption with log N_{HI}≳14.5 (e.g. D'Odorico et al. 2010; Boksenberg & Sargent 2015), corresponding approximately to overdensities of a few at $z \sim$ 3, probing only the densest few per cent of the cosmic volume. At lower H I column densities, the detection of associated C IV absorption peters out (Cowie & Songaila 1998).

The O VI species is expected to be a more sensitive tracer of metals in the low density IGM at $z \sim$ 2–3 (e.g. Cen & Chisari 2011), but the relevant absorption lines occur in the same wavelength range as the

---

[1] We define the overdensity as $(\delta + 1) \equiv \rho/\bar{\rho}$.

Lyman forest, which makes the detection of weak O VI absorption challenging (e.g. Bergeron et al. 2002; Carswell, Schaye & Kim T-S. 2002; Simcoe, Sargent & Rauch 2004).

Moved by the motivation of directly investigating the metal enrichment of the IGM down to the mean density, we have repeated the enterprise of obtaining an ultra-high SNR quasar spectrum (dubbed the *deep* spectrum) using UVES at the ESO Very Large Telescope, 15 yr after the observation of the first and only extremely high SNR quasar spectrum of B1422+231.

In this paper, we describe the observation campaign, the data reduction and analysis of the UVES deep spectrum of the quasar HE0940-1050 ($z_{em} = 3.0932$) in Section 2. Section 3 is dedicated to the statistics of the lines and the comparison with previous samples. In Section 4, we present the C IV detection rate and discuss the connection with galaxies. Section 5 addresses the core topic, the metallicity of the IGM. The final discussion and the conclusions are drawn in Section 6.

The computation of the POD for C IV and O VI will be reported in a further paper. The thermal properties of the IGM at $z \sim 3$ have been studied with the Lyα forest of the deep spectrum in Rorai et al. (2016).

Throughout this paper, we assume $\Omega_m = 0.26$, $\Omega_\Lambda = 0.74$ and $h \equiv H_0/(100 \, \mathrm{km \, s^{-1} \, Mpc^{-1}}) = 0.72$.

2 DATA ACQUISITION AND TREATMENT

We carefully chose the target for the deep spectrum to address two main requirements: (i) an emission redshift $z_{em} \sim 3$, representing a trade-off between the need to probe the low-density medium (at higher redshift the same column density corresponds to lower density) and that of avoiding the excessive crowding in the Lyα forest (which increases with redshift); (ii) a line of sight free from Damped Lyα systems, whose presence would significantly decrease the portion of Lyα forest available for our study.

The selection was limited to the quasars observed for the UVES Large Programme (Bergeron et al. 2004, from now on UVES LP) because they were all picked out to be bright, Damped-free targets and they have available good quality spectra. We chose the quasar HE0940-1050 ($z_{em} \simeq 3.0932$) which is the brightest quasar of the sample fulfilling our requirements.

Aiming at detecting at 3σ confidence level lines with column densities $\log N_{CIV} \simeq 11.5$ ($\log N_{OVI} \simeq 12.2$),[2] we computed the required minimum SNR to be ~ 205 and 90 per resolution element in the C IV and O VI forests respectively, using the formula (Herbert-Fort et al. 2006):

$$\mathrm{SNR} \simeq \frac{3 \, \lambda_{r,X}}{c \, w_{r,X}} \sqrt{4.242\,64 \, b \, \Delta v} \tag{2}$$

where, $\lambda_{r,X}$ and $w_{r,X}$ are the rest frame wavelength and equivalent width of transition X, respectively, c is the speed of light, b is the Doppler parameter of the lines (assumed to be $\sim 10 \, \mathrm{km \, s^{-1}}$), and Δv is the velocity resolution element in km s^{-1}. The equivalent width of the line is then converted into a column density assuming

---

[2] If not otherwise specified, the sensitivities mentioned throughout the paper always refer to the strongest line of the doublet: C IV λ 1548 Å and O VI λ 1032 Å.

Table 1. Journal and settings of observations.

Prop. id	Date	Setup (nm)	Slit (as)	CCD binning	No. of frames	T_{exp} (s)
166.A-0106[a]	2001 Feb	346–580	1.0	2×2	4	14 400
		437–860	1.0	2×2	4	14 400
079.B-0469[b]	2007 Jun	390–564	1.0	2×2	2	6000
185.A-0745[c]	2012 Mar–Apr	390–580	0.8	1×1	3	13 200
		390–585	0.8	1×1	10	47 600
092.A-0170[d]	2013 Dec	390–564	1.0	2×2	1	4565
	2014 Jan–Mar	390–564	1.0	2×2	32	146 080

Notes. [a]Bergeron et al. (2004); [b]Misawa, Charlton & Eracleous (2014); [c]Molaro et al. (2013), [d]our proposal.

the linear regime of the curve of growth:

$$N(X) = 1.13 \times 10^{20} w_{r,X}/(f_X \lambda_{r,X}^2) \tag{3}$$

where, f_X is the oscillator strength of transition X.

Based on these computation, we proposed and obtained 43 h of observations with UVES (Dekker et al. 2000) at the ESO VLT. The programme was carried out between 2013 December and 2014 March, adopting a slit of 1 arcsec, the CCD binned 2×2 and using the dichroic standard setup with the blue arm centred at 390 nm and the red arm centred at 564 nm. This configuration allows us to cover the two regions of interest with one observation (bluewards of 360 nm the quasar flux is almost completely absorbed by the break due to a Lyman limit system).

To create our final spectrum we used also all the other observations of HE0940-1050 already present in the ESO UVES archive, for a total of 64.4 h both in the region of the Lyman α/Lyman β forests and of the C IV forest on the red side of the quasar Lyman α emission. The journal of observations and the specific settings adopted by the different programmes are reported in Table 1.

2.1 Data reduction

Our data plus all the data of the same object available in the ESO UVES archive were reduced with the most recent version of the UVES pipeline (v. 5.4.3, Ballester et al. 2000) in the context of the Reflex workflow environment. The set of spectra observed at higher resolution (see Table 1) was degraded to the resolution of all the other spectra. All spectra were rebinned to 0.003 nm in the 346 and 390 setups, to 0.0035 nm in the 437 setup, and to 0.0045 nm in the 564, 580, 585 setups.

A dedicated software developed by us (see Cupani et al. 2015a,b) for the future VLT spectrograph ESPRESSO (Pepe et al. 2014) has been used in order to:

(i) correct the blaze response and normalize each 1-D extracted, (vacuum heliocentric-)wavelength calibrated order of each spectrum. In this way all the spectral orders are brought to the same flux scale with the appropriate uncertainties for each pixel;

(ii) co-add in a single operation all the orders of all the spectra with a drizzling technique (e.g. Gonzaga et al. 2012) to the final wavelength grid with a 2.5 km s^{-1} pixel size.

The flux in each velocity bin of the final spectrum is obtained from a weighted average of the contributions of all pixels from the original exposures that (at least partially) overlap the bin. For each contribution, the weights are proportional to the overlap and inversely proportional to the variance. The co-adding recipe also monitors the SNR and the error statistics of the co-added spectrum, comparing the latter to the RMS of the contributions, and raises
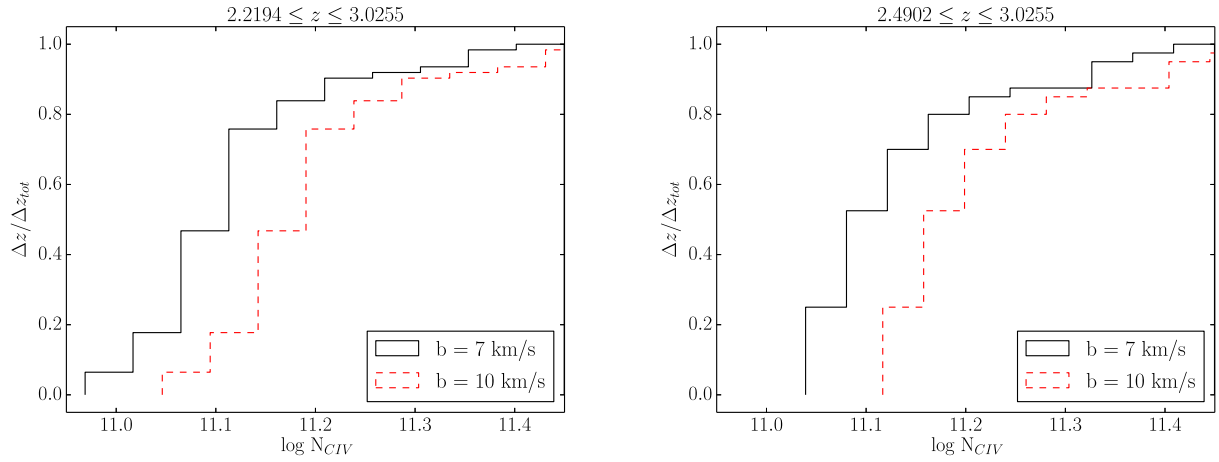
Figure 1. Cumulative fraction of two redshift ranges in the C IV forest (left-hand panel: 2.2194 ≲ z ≲ 3.0255 and right-hand panel: 2.4902 ≲ z ≲ 3.0255) for which the deep spectrum is sensitive at 3σ to C IV λ 1548 Å lines with a column density down to the reported limits (see Table 2). The sensitivity limits were computed assuming a Doppler parameter $b = 7.0 \, \mathrm{km \, s^{-1}}$ (solid black line) and $b = 10.0 \, \mathrm{km \, s^{-1}}$ (dashed red line). The definition of the two considered redshift ranges is reported in the text.

a flag when a significant discrepancy occurs, performing a kappa-sigma clipping (at a 3.5σ level) to amend any remaining defect in the reduced spectra.

The final spectrum covers the wavelength range λλ 305–702 nm in the vacuum-heliocentric reference system. The SNR – per $R = 45\,000$ resolution element – is 120–500 and 320–500 in the O VI/Lyα region and in the C IV region (outside the Lyα forest), respectively. The quality of the spectrum not only fulfills but exceeds the goals that we proposed for the project, allowing us investigate even lower metallicity gas than expected, as we will see in the following sections.

2.2 Detection and fit of metal and hydrogen lines

C IV doublets in our deep spectrum were looked for by eye in the region redwards of the Lyα emission plus $1000 \, \mathrm{km \, s^{-1}}$ and up to $5000 \, \mathrm{km \, s^{-1}}$ from the C IV emission to avoid contamination from the Lyα forest and the proximity effect from the quasar, respectively. This spectral portion corresponds to the redshift range 2.2194 ≲ z ≲ 3.0255.

In Fig. 1 (left-hand panel) we report the cumulative fraction of the above redshift range which is sensitive at 3σ level to C IV λ 1548 Å lines with a column density down to the given values. The column density limits were computed using equations (2) and (3) assuming a Doppler width of $b = 7.0 \, \mathrm{km \, s^{-1}}$ (*solid line*) and $b = 10.0 \, \mathrm{km \, s^{-1}}$ (*dashed line*) and computing the spectrum SNR in bins of 10 Å. The adopted b parameters are the mean observed value (see the end of this section) and the typical value assumed as a threshold to distinguish between Hydrogen and metal absorption lines, respectively. All the sensitivity values are reported in Table 2. Considering the case with $b = 7.0 \, \mathrm{km \, s^{-1}}$, the whole redshift range is sensitive to lines with column densities down to $\log N_{\mathrm{CIV}} \simeq 11.4$. However, ∼93 per cent of the considered redshift range is sensitive to lines down to $\log N_{\mathrm{CIV}} \simeq 11.3$, the less sensitive region corresponds to the gap in the UVES red arm for the 564 nm setup (2.6171 ≤ z ≤ 2.6817). Furthermore, ∼66 per cent of the redshift path is sensitive to lines down to $\log N_{\mathrm{CIV}} \simeq 11.1$.

In order to identify C IV doublets we used as a first guess the list of detected lines in the UVES LP spectrum by D'Odorico et al. (2010).

Table 2. Fraction of the C IV reported redshift range which is sensitive to C IV λ, 1548 Å lines with column densities down to the reported limits. The values are computed for Doppler parameters of 7 and $10 \, \mathrm{km \, s^{-1}}$.

| $\log N_{\mathrm{CIV}}$	$\Delta z / \Delta z_{\mathrm{tot}}$	
2.2194 ≲ z ≲ 3.0255		
	$b = 7.0$	$b = 10.0$
10.90	0.000	0.000
10.95	0.024	0.000
11.00	0.067	0.008
11.05	0.258	0.032
11.10	0.657	0.121
11.15	0.812	0.437
11.20	0.848	0.725
11.25	0.920	0.828
11.30	0.928	0.848
11.35	0.976	0.920
11.40	1.0000	0.953
11.45	1.0000	0.976
11.50	1.0000	1.0000
11.55	1.0000	1.0000
2.4902 ≲ z ≲ 3.0255		
$\log N_{\mathrm{CIV}}$	$\Delta z / \Delta z_{\mathrm{tot}}$	
	$b = 7.0$	$b = 10.0$
10.90	0.000	0.000
10.95	0.000	0.000
11.00	0.024	0.000
11.05	0.217	0.000
11.10	0.608	0.093
11.15	0.747	0.386
11.20	0.771	0.639
11.25	0.879	0.771
11.30	0.891	0.771
11.35	0.964	0.879
11.40	1.0000	0.930
11.45	1.0000	0.964
11.50	1.0000	1.0000
11.55	1.0000	1.0000
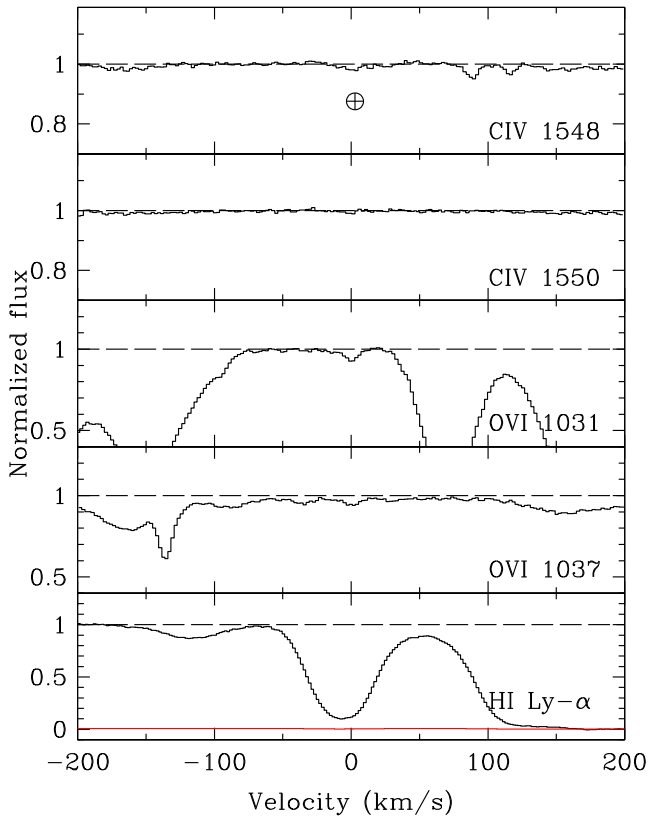
Figure 2. Plot of the absorption system at $z_{abs} \simeq 2.857\,951$ (redshift determined by O VI and corresponding to $v = 0\,\mathrm{km\,s^{-1}}$). A weak telluric line falls at the wavelength of the possible C IV λ 1548 absorption. Note that in the panels showing C IV $\lambda\lambda$ 1548, 1550 Å and O VI $\lambda\lambda$ 1032, 1037 Å the *y*-axis is zoomed to see better the weak absorptions.

Then we carried out a blind survey searching for more C IV doublets and finally, we looked for the weakest systems taking into account their association with Lyα lines. We detected 102 C IV λ 1548 lines, of which 32 are new detections with respect to the LP starting list. It is interesting to note that of the 32 new detections, 15 are weak isolated lines, which are the main target of this study.

The H I lines were identified and fitted independently of their association with metal lines. To obtain reliable H I column densities, the analysis was focused on the redshift range for which we had at least the H I Lyα and Lyβ transitions, corresponding to $2.4902 \lesssim z \lesssim 3.0255$. Metal contaminants in the Lyα forest were sought by:

(i) including lines from ions found redwards of the Lyα emission line, notably Si II and Fe II;

(ii) including other ions in systems found redwards of the Lyα emission line, e.g C II if Si II is present, Si III and Si IV if C IV is present;

(iii) identifying doublets of C IV, Si IV, Mg II, and anything associated with them, especially for narrow lines;

(iv) treating a feature as something other than Lyα if the corresponding Lyβ feature was too weak to be consistent with the oscillator strengths.

Hereafter, the metallicity analysis will be carried out in the reduced redshift range $2.4902 \lesssim z \lesssim 3.0255$. As shown in Fig. 1 (right-hand panel), $\sim$60 per cent of this interval is sensitive to C IV lines with $\log N_{\mathrm{CIV}}$ down to 11.1, $\sim$90 per cent to lines down to $\log N_{\mathrm{CIV}} \simeq 11.3$ and in the whole interval we can detect at 3σ C IV lines with column density down to 11.4 (these values are valid for a
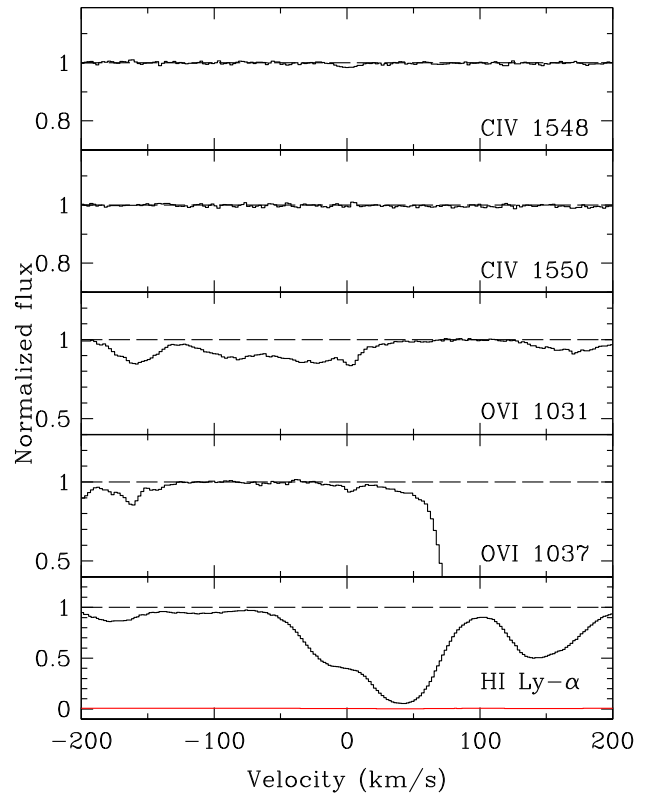
Figure 3. Plot of the absorption system at $z_{abs} \simeq 2.898\,765$ (redshift determined by O VI). Note that in the panels showing C IV $\lambda\lambda$ 1548, 1550 Å and O VI $\lambda\lambda$ 1032, 1037 Å the *y*-axis is zoomed to see better the weak absorptions.

Doppler parameter $b = 7.0\,\mathrm{km\,s^{-1}}$, see Table 2). The total number of detected C IV λ 1548 falling in the reduced redshift range is 69.

Simulations (e.g. Cen & Chisari 2011; Shen et al. 2013) predict that O VI is a better tracer of metals than C IV in the low density gas at these redshifts. However, due to the location of the O VI doublet ($\lambda\lambda$1032, 1037 Å) in the Lyα/Lyβ forests, its identification becomes extremely challenging. We have carried out: first a search for the O VI lines associated with the already detected C IV absorptions, and then a search to find the weakest O VI features using the association with H I Lyα absorptions. We considered as *detections* only those for which both components of the O VI doublet were identified. However, in most cases we found only one of the two components of the doublet. We defined the latter occurrences as *possible detections*[3] to distinguish them from those where we could just set an upper limit to the value of N_{OVI} (see below). We found three O VI detections (see Figs 2, 3 and 4, and Table 3) of which two were not associated with previously identified C IV lines: the system at $z_{abs} \simeq 2.898\,765$ shows a very weak C IV λ 1548 line, while the system at $z_{abs} \simeq 2.857\,951$ does not show a detectable C IV absorption (there is a weak telluric line falling exactly at this wavelength). Besides these systems, we have also 15 O VI possible detections, of which 6 do not show an associated C IV line. The plots of all O VI possible detections are shown in the Appendix.

The determination of the O VI sensitivity limits for the considered redshift range is extremely difficult due to the large number of Lyα, Lyβ and metal lines. We obtained an estimate of the 2σ O VI limits by placing doublets with Doppler width $b = 8\,\mathrm{km\,s^{-1}}$ in the

---

[3] Note that in the following analysis *possible detections* were counted as upper limits.
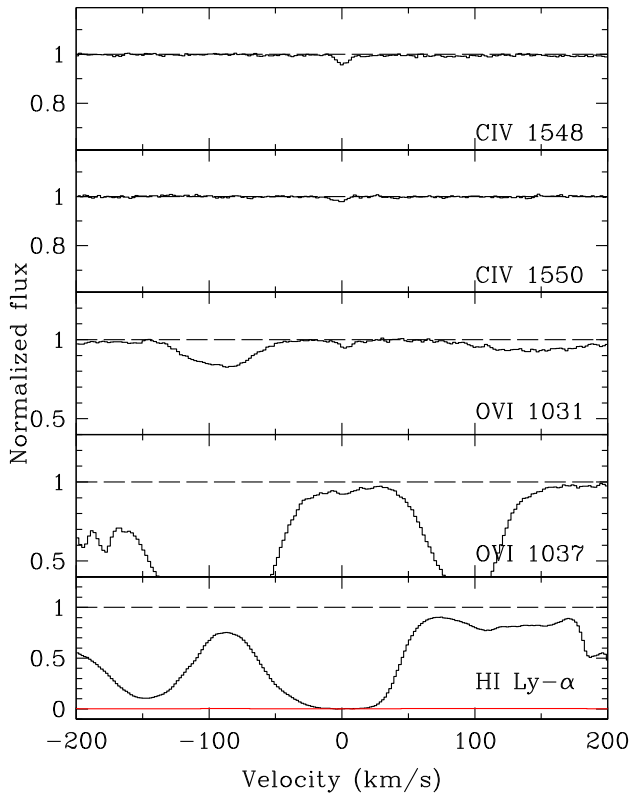
Figure 4. Plot of the absorption system at $z_{\mathrm{abs}} \simeq 3.024\,783$ (redshift determined by C IV). Note that in the panels showing C IV $\lambda\lambda$ 1548, 1550 Å and O VI $\lambda\lambda$ 1032, 1037 Å the *y*-axis is zoomed to see better the weak absorptions.

Table 3. Parameters obtained from the fit of the detections of O IV doublets in the range $2.4902 \lesssim z \lesssim 3.0932$.

z_{abs}	σ_z	b (km s^{-1})	σ_b (km s^{-1})	$\log N$	$\sigma_{\log N}$
2.857 951	0.000 005	6.6	0.6	12.44	0.03
2.898 767	0.000 03	4.1	0.5	12.39	0.03
3.024 823	0.000 01	8.2	1.2	12.38	0.04

Lyα/Lyβ forest at a series of redshifts in steps of 6.7 Å.[4] Using RDGEN (Carswell et al. 2014), we increased the column density in small steps until at least one of the lines was just too strong to be consistent with the data at the 2σ level. The result is shown in Fig. 5.

The fit of the lines was carried out both with the Voigt profile fitting code VPFIT (Carswell & Webb 2014) and the *fitlyman* context of the ESO MIDAS package (Fontana & Ballester 1995), for comparison. In general, there are no significant differences between the results of the two fits. In the following computation we adopt the results obtained with VPFIT.

Finally, to complete our measurement, we have determined the 3σ upper limits to C IV and O VI column densities at the redshift of all the H I lines in our sample down to $\log N_{\mathrm{HI}} \simeq 13.5$, using formulae in equations (2) and (3). Doppler parameter values $b = 7.0$ and 8.0 km s^{-1} were adopted for C IV and O VI, respectively. Those values are the mean Doppler parameters fitted to detected C IV lines with $\log N_{\mathrm{CIV}} < 12.0$ in our sample and to the detections
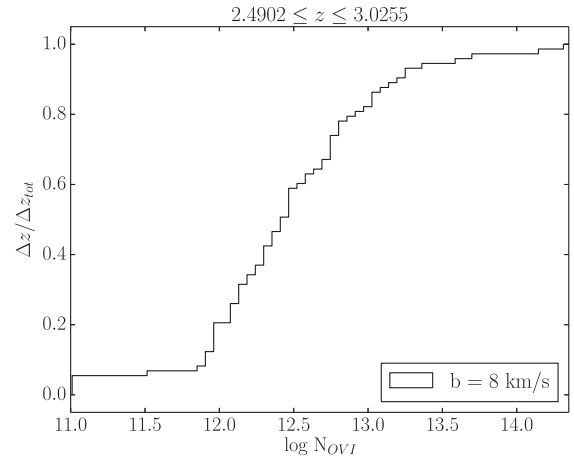
Figure 5. Cumulative fraction of the redshift range in the O VI forest for which the deep spectrum is sensitive at 2σ to either line of the doublet with a column density down to the reported limits. The sensitivity limits were computed assuming a Doppler parameter $b = 8.0$ km s^{-1}.

and possible detections of O VI, respectively. The list of all detected C IV absorption lines is reported in Table 4.

3 COLUMN DENSITY DISTRIBUTION FUNCTIONS

The column density distribution function (CDDF), $f(N)$, is defined as the number of lines per unit column density and per unit redshift absorption path, dX (Tytler 1987). The CDDF is a fundamental statistics for absorption lines, similar for many aspects to the luminosity function for stars and galaxies.

The redshift absorption path is used to remove the redshift dependence in the sample and put everything on a comoving coordinate scale. In the assumed cosmology it is defined as:

$$\mathrm{d}X \equiv (1+z)^2[\Omega_{\mathrm{m}}(1+z)^3 + \Omega_{\Lambda}]^{-1/2}\mathrm{d}z. \tag{4}$$

With the adopted definition, $f(N)$ would be the same at any redshifts for a non-evolving population of absorbers.

In Fig. 6 the CDDF for the C IV lines detected in the deep spectrum is compared with the CDDF computed for the C IV lines detected by ESSP00[5] and with the CDDF computed for the sample of more than 1000 lines by D'Odorico et al. (2010). In the three samples, lines closer than 50 km s^{-1} have been merged into a single line with column density equal to the sum of the column densities and redshift equal to the column density weighted mean of the original redshifts. This operation was carried out in order to avoid spurious effects in the low column density regime due to the weak C IV components introduced by the process of fitting complex systems (note that the three samples were fitted with different softwares).

It is evident from Fig. 6 that, although the three samples cover different redshift intervals, there are no significant differences for $\log N_{\mathrm{CIV}} \geq 12.3$. In the low column density regime, our result confirms the result obtained by ESSP00 with the completeness correction and extends the increasing trend down to $\log N_{\mathrm{CIV}} \simeq 11.3$. On the other hand, the comparison with the lower SNR sample shows the significant improvement obtained with the deep spectrum at the lowest column densities.

Table 4. Parameters obtained from the fit of all detected C IV lines in the range $2.2194 \lesssim z \lesssim 3.0932$.

| z_{abs}	σ_z	b (km s^{-1})	σ_b (km s^{-1})	$\log N$	σ_{logN}
2.220 038	0.000 002	7.2	0.3	12.48	0.02
2.220 242	0.000 001	7.3	0.2	12.63	0.01
2.220 5064	0.000 0008	7.64	0.08	13.502	0.005
2.220 6458	0.000 0005	5.79	0.05	13.558	0.004
2.221 070	0.000 008	12.5	1.0	12.52	0.04
2.221 312	0.000 001	6.2	0.3	13.19	0.07
2.221 42	0.000 02	11.9	2.2	13.2	0.1
2.221 608	0.000 001	6.5	0.1	13.23	0.02
2.328 888	0.000 009	4.9	0.2	13.1	0.14
2.328 957	0.000 005	5.0	0.5	13.40	0.07
2.329 1776	0.000 0006	11.9	0.1	14.390	0.003
2.329 4592	0.000 0005	7.89	0.08	13.908	0.003
2.329 641	0.000 007	3.9	1.2	11.8	0.11
2.329 929	0.000 002	5.5	0.1	13.20	0.02
2.330 057	0.000 004	7.5	0.9	13.21	0.09
2.330 294	0.000 002	9.0	0.9	13.7	0.16
2.330 49	0.000 09	19.8	10.7	13.7	0.27
2.330 669	0.000 002	5.1	0.4	13.24	0.05
2.330 71	0.000 02	15.9	1.1	13.96	0.14
2.330 77	0.000 01	61.3	4.7	13.7	0.12
2.331 130	0.000 004	14.6	1.0	13.49	0.07
2.331 239	0.000 001	5.6	0.3	12.95	0.04
2.331 482	0.000 003	5.3	0.6	12.38	0.06
2.331 623	0.000 008	5.6	1.3	11.96	0.12
2.332 278	0.000 007	12.5	1.1	12.08	0.03
2.332 57	0.000 01	5.0	1.6	11.41	0.08
2.392 362	0.000 005	14.1	0.7	12.11	0.02
2.408 887	0.000 002	7.6	0.4	12.89	0.06
2.408 994	0.000 004	13.8	0.2	13.46	0.02
2.428 289	0.000 006	22.9	0.7	12.44	0.01
2.450 22	0.000 01	9.6	1.9	11.67	0.06
2.450 57	0.000 01	9.9	1.5	11.80	0.04
2.450 90	0.000 01	5.2	2.1	11.37	0.09
2.516 23	0.000 01	32.6	1.4	12.59	0.02
2.516 660	0.000 001	9.2	0.2	12.53	0.01
2.529 09	0.000 01	6.2	2.0	11.51	0.08
2.566 401	0.000 005	6.0	0.7	11.97	0.03
2.596 45	0.000 02	15.9	2.3	11.74	0.05
2.613 624	0.000 002	9.3	0.3	12.52	0.01
2.613 89	0.000 01	8.6	0.9	11.81	0.03
2.642 776	0.000 008	14.9	1.0	12.48	0.02
2.643 171	0.000 002	11.2	0.3	12.984	0.009
2.643 64	0.000 01	22.2	1.8	12.48	0.03
2.657 911	0.000 002	14.2	0.2	13.26	0.01
2.657 949	0.000 001	4.9	0.3	12.84	0.02
2.659 252	0.000 006	6.9	0.8	11.93	0.03
2.667 18	0.000 04	11.4	2.1	12.6	0.17
2.667 44	0.000 03	12.1	3.6	13.1	0.19
2.667 632	0.000 015	9.7	0.9	13.2	0.12
2.667 915	0.000 002	12.0	0.2	13.374	0.008
2.711 67	0.000 015	10.	2.	11.61	0.06
2.771 388	0.000 004	9.6	0.5	12.41	0.02
2.785 94	0.000 01	10.73	1.2	11.77	0.04
2.810 878	0.000 003	12.23	0.4	12.49	0.01
2.823 005	0.000 008	9.8	1.1	12.02	0.03
2.823 30	0.000 02	6.9	2.5	11.5	0.13
2.823 84	0.000 02	24.7	2.2	12.81	0.04
2.824 05	0.000 01	5.9	1.8	11.9	0.23
2.824 28	0.000 01	11.0	1.0	13.07	0.07
2.8245	0.0001	11.5	5.7	12.2	0.46
2.825 117	0.000 006	24.8	1.0	13.00	0.01
2.825 149	0.000 002	6.2	0.5	12.37	0.04

Table 4 *– continued*

z_{abs}	σ_z	b (km s^{-1})	σ_b (km s^{-1})	$\log N$	σ_{logN}
2.825 459	0.000 007	4.4	1.4	11.7	0.12
2.825 924	0.000 006	10.1	1.1	12.22	0.08
2.826 34	0.000 06	29.8	6.5	12.45	0.09
2.826 5569	0.000 0005	6.5	0.1	13.188	0.006
2.826 765	0.000 005	5.0	0.9	11.94	0.08
2.827 369	0.000 004	7.4	0.6	12.29	0.04
2.827 716	0.000 0015	5.5	0.3	12.60	0.02
2.828 0270	0.000 0008	11.3	0.1	13.38	0.01
2.828 064	0.000 008	51.5	1.0	13.630	0.009
2.828 344	0.000 002	7.4	0.3	12.72	0.02
2.828 868	0.000 004	9.1	0.3	12.77	0.02
2.828 939	0.000 008	2.5	2.1	11.6	0.25
2.832 878	0.000 007	17.7	0.7	12.74	0.01
2.833 322	0.000 006	14.4	0.7	12.62	0.02
2.833 965	0.000 002	5.3	0.5	12.44	0.07
2.833 976	0.000 003	16.4	0.5	13.21	0.01
2.834 51	0.000 06	13.8	1.0	13.7	0.32
2.834 557	0.000 008	8.8	1.1	13.7	0.26
2.834 810	0.000 005	8.0	0.7	13.55	0.07
2.834 995	0.000 006	7.9	0.7	13.26	0.09
2.835 11	0.000 04	17.9	2.1	13.2	0.11
2.860 75	0.000 03	7.9	1.7	12.2	0.18
2.860 91	0.000 01	7.8	0.9	12.56	0.08
2.883 528	0.000 004	11.0	0.4	12.25	0.01
2.898 72	0.000 02	12.1	2.5	11.57	0.07
2.916 683	0.000 006	3.3	1.	11.7	0.1
2.916 856	0.000 02	22.1	1.	13.19	0.03
2.917 109	0.000 002	11.1	0.6	12.93	0.06
2.917 555	0.000 013	2.6	2.6	11.26	0.12
2.918 023	0.000 004	6.1	0.7	11.98	0.03
2.930 791	0.000 015	12.4	1.2	12.36	0.05
2.931 062	0.000 017	10.5	1.3	12.19	0.07
2.937 147	0.000 008	20.	1.	12.33	0.02
2.937 751	0.000 001	10.5	0.2	12.717	0.007
2.939 641	0.000 001	4.7	0.1	12.37	0.006
2.940 080	0.000 005	13.1	0.7	12.18	0.02
2.940 455	0.000 004	8.8	0.5	12.11	0.02
2.950 46	0.000 015	9.0	1.7	11.49	0.06
2.982 51	0.000 02	12.1	2.4	11.46	0.06
3.024 783	0.000 004	4.8	0.7	11.76	0.04
3.038 220	0.000 004	5.9	0.5	11.83	0.02
3.038 593	0.000 001	9.4	0.1	12.606	0.005

The CDDF of the H I lines is shown in Fig. 7. A comparison with the H I lines fitted in the quasars of the UVES LP shows significant differences for $\log N_{HI} < 12$. In both samples we have selected lines to have $10 \leq b \leq 200 \, \text{km s}^{-1}$ and errors on the column density $\sigma(N_{HI}) < 0.5 N_{HI}$ and on redshift $\sigma(z) < 8 \times 10^{-5}$ (corresponding to about 3 pixels).

4 C IV DETECTION RATE AND THE CONNECTION WITH GALAXIES

The main goal of this work is to shed light on the abundance and covering factor of metals in the low density gas. To this aim we have computed the detection rate of C IV lines (down to our observational limit) as a function of the column density of the associated H I absorption.

The association H I–C IV absorbers has been carried out in the following way. First, we have determined all the pairs H I–C IV absorber at velocity separations closer than $dv = 50 \, \text{km s}^{-1}$. This
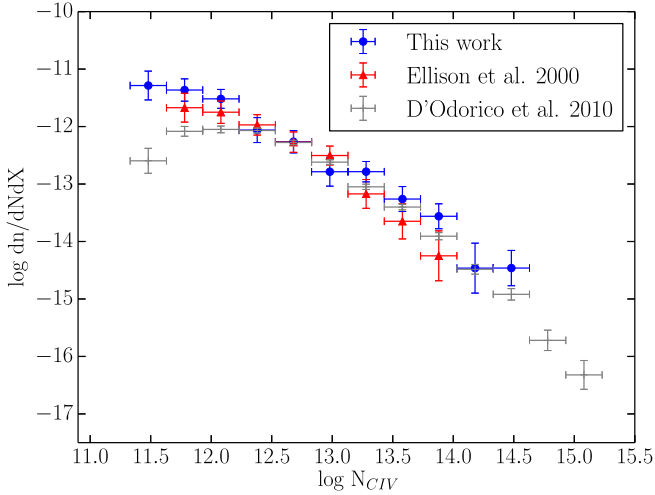
Figure 6. CDDF of C IV lines in the spectrum of HE0940-1050 (blue points). The bin-size is $10^{0.3} N_{CIV}$ cm^2 and the error bars are $\pm 1\sigma$, based on the number of points in each bin. Superposed are the CDDFs computed for the list of C IV lines detected by ESSP00 (red triangles) and for the C IV lines in D'Odorico et al. (2010, grey crosses). In the three samples, lines closer than 50 km s^{-1} have been merged (see text).
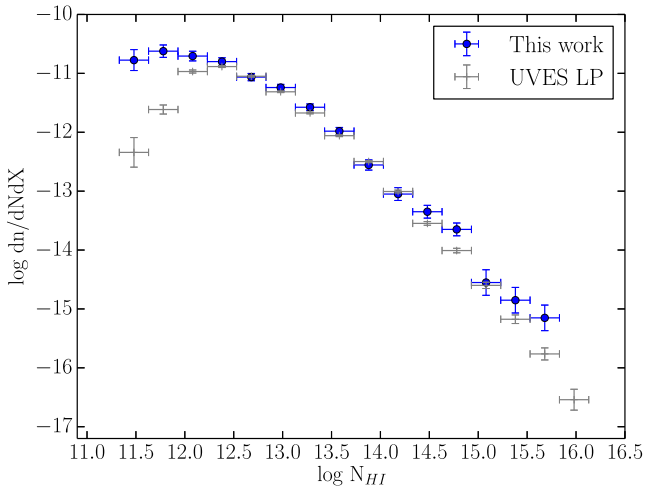
Figure 7. CDDF of H I lines in the spectrum of HE0940-1050 (blue points). The bin-size is $10^{0.3} N_{HI}$ cm^2 and the error bars are $\pm 1\sigma$, based on the number of points in each bin. Superposed is the CDDFs computed for the H I lines of the quasars in the UVES LP (D'Odorico et al. 2008, grey crosses).

is approximately the smallest velocity separation for which all C IV lines in our sample are associated with at least one H I line. Then, if the same C IV line was associated with multiple H I lines we kept only the closest association. Finally, if more than one C IV line was associated with the same H I line, we merged the C IV lines into a single system with column density equal to the sum of the column densities and redshift equal to the column density weighted mean of the original redshifts. The distribution of the velocity shifts between the associated H I and C IV lines is shown in Fig. 8.

Having obtained the final list of one to one associations between H I and C IV lines, the C IV detection rate was computed by dividing the number of H I lines with an associated C IV absorption in a given H I column density bin by the total number of H I lines in that bin. All the computed detection rates are dependent on the completeness limit of our sample which is $\log N_{CIV} = 11.4$ for the whole considered redshift range (see Section 2.2 for more details).

Figure 8. Distribution of the velocity shifts between associated H I and C IV lines.

Table 5. C IV detection rate down to our (conservative) detection limit of $\log N_{CIV} = 11.40$ in the spectrum of HE0940.

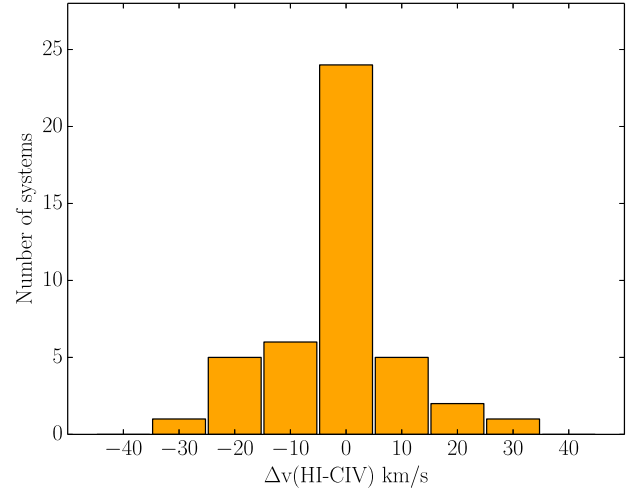| $\log N_{HI}$	No. of lines	No. of detection	Det. rate
≥ 15.0	16	16	1.00
[14.5: 15.0]	21	12	0.57
[14.0: 14.5]	28	12	0.43
[13.5: 14.0]	56	4	0.07
[13.0: 13.5]	98	2	0.02
≥ 14.8	22	22	1.00
[14.0: 14.8]	42	18	0.43
[13.5: 14.0]	56	4	0.07
[13.0: 13.5]	98	2	0.02

Our findings (summarized in Table 5) are consistent with the results of the first works on metals in the IGM (e.g. Cowie et al. 1995): above a column density of $\log N_{HI} \simeq 15$ all H I lines have associated C IV lines, while in the column density bin $14.5 \leq \log N_{HI} < 15$, 57 per cent of the observed H I absorptions have associated metals. Actually, thanks to our exceptional sample, we find a C IV detection rate of 100 per cent for $\log N_{HI} \geq 14.8$, while we can state that 43 per cent of H I lines with $14.0 \leq \log N_{HI} < 14.8$ have an associated C IV absorption. Below $\log N_{HI} \simeq 14.0$, we observe a drop with detection rates lower than 10 per cent. Of course, we have to take into account that our measurements are based on a single spectrum and that, in particular for $\log N_{HI} \lesssim 14.5\text{-}15$ there could be variations from one line of sight to the other.

In Fig. 9, we compare our result for the C IV detection rate with the fraction of H I lines which arises within $|\Delta v| < 300$ km s^{-1} (difference in redshift) and $D_{tran} < 300$ physical kpc (transverse separation) of star forming galaxies at $2 \lesssim z \lesssim 2.8$ as obtained by Rudie et al. (2012). The comparison shows that the metal detection rate for lines with $\log N_{HI} \geq 14.0$ is more than a factor of 2 larger than the fraction of H I lines tracing the circumgalactic medium (CGM) of the galaxies in the sample used by Rudie and collaborators. Those galaxies inhabit dark matter haloes of average mass $\sim 10^{12}$ M$_\odot$ and the fainter objects correspond to $0.25 L^*_{UV}$ (at $\langle z \rangle = 2.30$).

Our result points out that metals are diffused also outside the CGM of the considered galaxies. They could reside in filaments enriched by *in situ* star formation or in the outskirts of smaller, fainter galaxies which are not present in the sample of Rudie et al. (2012). Metals could also lie at larger distances than the 300 physical
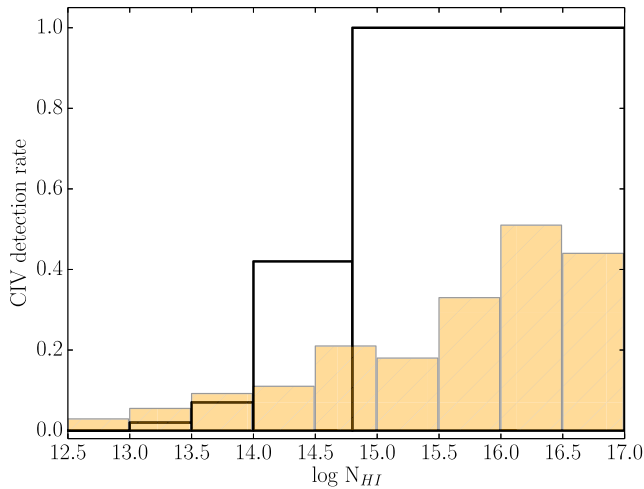
Figure 9. Detection rate of C IV absorbers (down to our detection limit of $\log N_{CIV} = 11.4$) as a function of the column density of the associated H I line (white, open histogram). The overplotted hatched histogram is the fraction of H I systems that arise within $|\Delta v| < 300 \,\mathrm{km\,s^{-1}}$ and $D_{tran} < 300$ physical kpc from LB galaxies (adapted from Rudie et al. 2012).

kpc assumed by Rudie and collaborators, possibly due to enrichment by earlier generations of galaxies. Hints of the fact that metals are widespread beyond the regions around galaxies were found also in previous observational works (e.g. Pieri, Schaye & Aguirre 2006; Martin et al. 2010).

5 THE METALLICITY OF THE IGM

Having computed the C IV detection rate as a function of the H I column density, we can ask ourselves if the drop that we observe below $\log N_{HI} \simeq 14.0$ in Fig. 9 is due to a real decrease of the metal enrichment of the IGM at those overdensities or if it could be ascribed to our limited sensitivity. In general, we would like to know which is the characteristic metallicity of the CGM/IGM gas at the investigated redshifts.

To this aim, we have generated a set of simple photoionization models using version 13.0 of CLOUDY, last described by Ferland et al. (2013). In the models, we have assumed a plane parallel slab of gas at a constant temperature T, ionized by the inbuilt Haardt & Madau UV background (Haardt & Madau 2001) at redshift $z = 2.8$. The computation stops when a given column density of H I is reached and the column densities of the studied ions are given in output (solar relative abundances are assumed). We built a grid of models varying overdensity and metallicity. The corresponding temperature T is defined by the temperature–density relation valid for the IGM (Hui & Gnedin 1997):

$$T = T_0(1 + \delta)^{\gamma - 1} \tag{5}$$

where we assume $T_0 = 10^4$ K and $\gamma = 1.5$ (following Becker et al. 2011). The total density is computed based on the mean density at the considered redshift and the considered overdensity. The H I column density used to stop the computation is determined using the formula by Schaye (2001):

$$N(\mathrm{H\,I}) \simeq 2.7 \times 10^{13} \mathrm{cm}^{-2} (1 + \delta)^{1.5 - 0.26(\gamma - 1)} T_{0,4}^{-0.26} \tag{6}$$

$$\Gamma_{-12}^{-1} \left(\frac{1 + z}{4}\right)^{9/2}$$

where we have adopted $T_{0,4} \equiv T_0/10^4 \mathrm{K} = 1$, $\Gamma_{-12} \equiv \Gamma/10^{-12} = 1$ and $\gamma = 1.5$, as above. All the model parameters are reported in Table 6.

Table 6. Parameters of the CLOUDY models. We adopted grid in overdensity and metallicity. Metallicity is not reported in the table, we considered metallicites with respect to solar $\log Z/Z_\odot = [-4.0, -3.5, -3.0, -2.5, -2.0, -1.5, -1.0]$. In each cell of the table, we report the total number density, the H I column density (both in log) and the temperature for the corresponding overdensity at $z = 2.8$. See text for more details.

| | $(\delta + 1)$ | | | | | |
	1.0	3.0	5.0	12.0	15.0	50.0
$\log n_H$	−5.02	−4.55	−4.33	−3.846	−3.95	−3.33
$\log N_{HI}$	13.33	13.98	14.29	14.81	14.94	15.66
$T/10^4$ K	1.0	1.7	2.2	3.5	3.9	7.1

In Fig. 10, we plot our observational results for C IV and O VI versus H I column densities for each absorber, together with the predictions of the photoionization models described above. In the plots, we empirically identify three possible regimes. At $\log N_{HI} \geq 14.8$ (corresponding to $(\delta + 1) \simeq 11.8$ at $z = 2.8$), we are probing regions permeated by metals with $-3 \lesssim \log Z/Z_\odot \lesssim -1$, likely tracing the CGM close to galaxies. The range $14.0 \leq \log N_{HI} < 14.8$ is where observationally we are most sensitive to the very low metallicity gas: what we observe is that ∼60 per cent of absorbers are enriched to metallicities $-3 \lesssim \log Z/Z_\odot \lesssim -1$ (considering upper limits as measurements); while ∼40 per cent of absorbers are characterized by metallicities $\log Z/Z_\odot \lesssim -3$, mostly traced by C IV upper limits. Assuming that all C IV upper limits would trace metallicities $\lesssim -3$, a lower limit of 38 per cent of absorbers would have $-3 \lesssim \log Z/Z_\odot \lesssim -1$. The possible O VI detections (filled pink dots) and the single detection (filled blue square) observed in this H I column density regime trace a slightly lower metallicity interval ($-3 \lesssim \log Z/Z_\odot \lesssim -2$). For $\log N_{HI} < 14.0$ our measurements of C IV lines are no longer sensitive to metallicities $\log Z/Z_\odot \lesssim -3$ (and going down in N_{HI}, the limit rises above $\log Z/Z_\odot \sim -2$). As a consequence, even if the gas traced by those H I absorbers was enriched at the same level as the gas traced by larger H I column densities, our observations could not detect the associated C IV lines. On the other hand, more stringent upper limits on the metallicity in this overdensity regime can be put using O VI (lower panel of Fig. 10) for which we find that ∼88 per cent of the absorbers have metallicities $\log Z/Z_\odot < -2$ and, in particular, ∼24 per cent of absorbers have $\log Z/Z_\odot < -3$.

With the caveat that we are dealing with a small sample, we carried out a more detailed analysis of the metallicity of the gas probed by the H I absorption lines with $14.0 \leq \log N_{HI} < 14.8$, range in which our observations are more sensitive to the very low metallicities. This column density interval, when translated into overdensities with equation (6), corresponds to $3.1 \leq (\delta + 1) \leq 11.8$ at $z = 2.8$. In the considered column density interval, 42 H I lines were detected, of which 18 have an associated C IV absorber, while for the remaining 24 lines we have determined an upper limit to $\log N_{CIV}$.

The sample of H I–C IV pairs has been compared with the results of our CLOUDY models at redshift $z = 2.8$, computed for the finer metallicity grid: $\log Z/Z_\odot = [-4.0, -3.5, -3.0, -2.5, -2.0, -1.5, -1.0]$. The results of this comparison are shown in form of histogram of the fraction of lines falling in each metallicity bin in Fig. 11. The figure shows that the majority of the lines falls in the bin at $\log Z/Z_\odot = [-3.5, -3.0]$, but the majority of the C IV detections falls in the range of metallicities $\log Z/Z_\odot = [-2.5, -2.0]$. The median of the distribution of lines falls in the bin $\log Z/Z_\odot = [-3.0, -2.5]$.
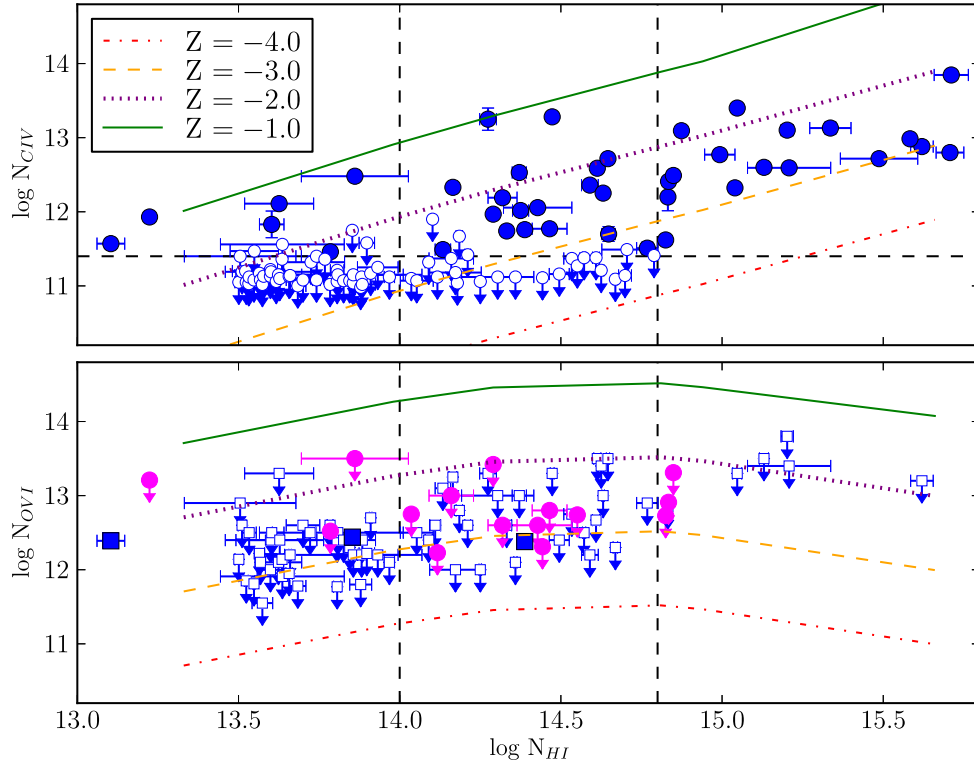
Figure 10. Upper panel: measurements (blue filled dots) and upper limits (open dots) of $\log N_{\mathrm{CIV}}$ as a function of the associated H I column density for our sample of absorbers. The horizontal dashed black line marks the (conservative) sensitivity limit $\log N_{\mathrm{CIV}} = 11.4$. Lower panel: measurements (blue filled squares), possible detections (pink filled dots) and upper limits (open squares) of $\log N_{\mathrm{OVI}}$ as a function of the corresponding H I column density. Upper limits have not been measured for $\log N_{\mathrm{HI}} < 13.5$. Overplotted are the corresponding column densities obtained from our photoionization models at $z = 2.8$; different lines correspond to different metallicities as marked in the figure. The two dotted vertical lines have been drawn at column densities $\log N_{\mathrm{HI}} = 14$ and 14.8 corresponding at $z = 2.8$ to $(\delta + 1) = 3.1$ and 11.8, respectively. See the text for more details.
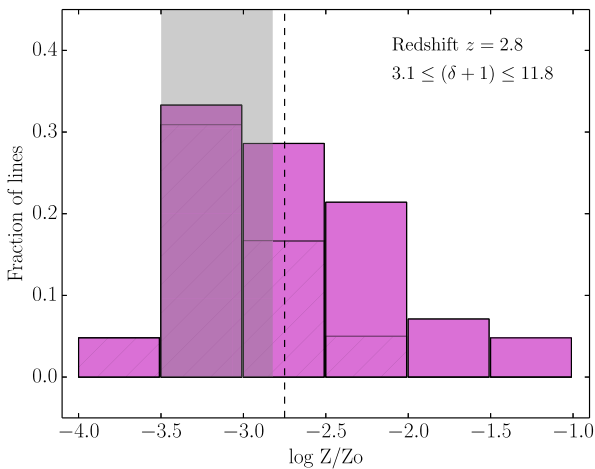
Figure 11. Fraction of observed C IV–H I absorbers with $14 \leq N_{\mathrm{HI}} \leq 14.8$ falling in different metallicity bins, when compared with CLOUDY predictions at $z = 2.8$. The hatched histograms correspond to the contribution of upper limits in each metallicity bin. The grey band is the prediction for the median [C/H] abundance computed with equation (1) by S03 for the considered overdensity range. See text for more details.

5.1 Comparison with POD results

ESSP00 estimated the relation between τ_{HI} and τ_{CIV} with the POD method using the extremely high SNR spectrum of B1422+231. Using a simple simulation, they showed that the POD result could

be reproduced only assuming that more metals than those directly detected were present. In particular, they assumed that all lines with $\log N_{\mathrm{HI}} \geq 14.5$ had an associated C IV line with at least $\log N_{\mathrm{CIV}} = 12.0$ and that all weak Lyα lines ($\log N_{\mathrm{HI}} < 14.5$) were enriched with a constant $\log$ C IV/H I $= -2.6$.

We have verified the validity of those conditions for our sample, starting from the hypothesis that the POD method is a cumulative technique. Thus, we can compute the total column density in C IV corresponding to a certain H I column density range and divide it by the number of H I lines to obtain the average C IV column density to be compared with ESSP00. First, all the H I lines in our sample with $\log N_{\mathrm{HI}} \geq 14.8$ have an associated C IV line with $\log N_{\mathrm{CIV}} \geq 12.0$. In the range of H I column densities $14.5 \leq \log N_{\mathrm{HI}} < 14.8$, we have computed the average C IV column density to be $11.97 \leq \log N_{\mathrm{CIV}} \leq 12.02$. The lower limit is obtained assuming that the H I lines without a C IV detection have zero C IV and the upper limit considering the C IV upper limits as measurements. On the other hand, for the H I lines with $13.5 \leq \log N_{\mathrm{HI}} < 14.5$ and adopting the same assumptions described above the average ratio varies between $-2.16 \leq \log$ C IV/H I ≤ -2.08. This implies that with our data we have directly detected the metals that ESSP00 found statistically applying the POD method.

In Fig. 11, our result obtained through the direct detection (or non-detection) of C IV lines has been compared with the median [C/H] abundance derived from the POD analysis by S03 and computed with equation (1) at the redshift and overdensities reported in the figure. The two median abundances are in good agreement, if we take into account all the uncertainties derived by the rough

modelling adopted in our work and also introduced by the conversion of the observed quantities into the [C/H] abundance in S03.

The POD analysis for the spectrum of HE0940-1050 will be presented in a forthcoming paper (D'Odorico et al., in preparation).

5.2 Volume filling factors

In order to have a more physical insight on the volume filling factors of the metal enriched gas, we analysed the output of a hydrodynamic simulation run with the GADGET-III code (Springel 2005), presented among the reference set of simulations in Viel et al. (2013). This simulation has reasonably well converged flux statistics for the Lyα forest and evolve a standard concordance cosmological model with 2×512^3 gas and dark matter particles in a periodic box of linear size $60\,h^{-1}$ comoving Mpc, while the IGM thermal history is in agreement with observational data. The gas particle distribution extracted at $z = 2.8$ is then interpolated on a grid using a Counts in Cells scheme that allows us to obtain an overdensity value over a grid of 512^3 points.

The overdensity values are reported in Fig. 12 in the form of per centage of volume occupied in bins of $\Delta[\log(1 + \delta)] = 0.01$ (solid line). However, since the reference simulation that we used is likely to be not perfectly converged in terms of density probability distribution function, we decided to overplot also the results obtained from a higher resolution study by Bolton & Becker (2009, dashed curve). For the densities of interest here, there is a small but not negligible difference between the two curves and quoted values conservatively bracket the uncertainties between the two results.

In the reference simulation box, the overdensities $3.1 \leq (\delta + 1) < 11.8$ (corresponding to the column density range $14.0 \leq \log N_{\mathrm{HI}} < 14.8$ at $z = 2.8$) occupy $\sim$4.7 per cent of the volume. Using the per centage of absorbers observed at different metallicities, we estimate that $\sim$2.8 per cent of the volume is enriched at $\log Z/Z_{\odot} \gtrsim -3$ and $\sim$1.9 per cent of the volume has a metallicity $\log Z/Z_{\odot} < -3$. If we extend our analysis to the mean density (corresponding in Fig. 10 to $\log N_{\mathrm{HI}} \sim 13.5$) then, the probed volume would increase to $\sim$17.4 per cent. Assuming the same percentages of absorbers at the different metallicites hold to this lower densities,
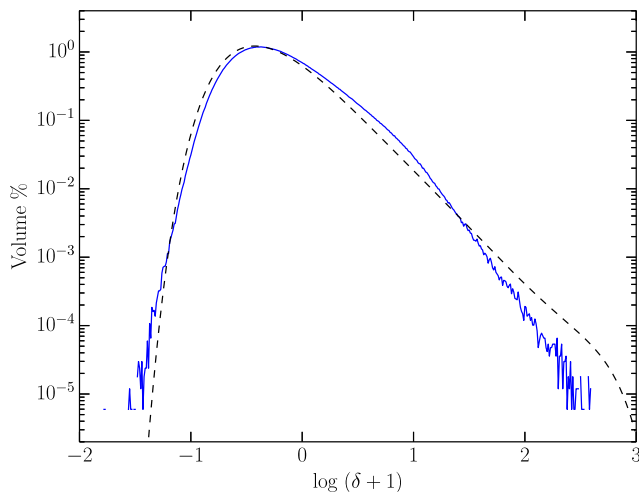
Figure 12. Percentage of volume occupied by a given overdensity computed from a cosmological hydrodynamical simulation box of 60 h^{-1} comoving Mpc at $z = 2.8$ (solid line, Viel et al. 2013). The overplotted curve (dashed line) is the result of a fit obtained from the higher resolution runs of Bolton & Becker (2009). See text for more details. Percentages are given in bins of $\Delta[\log(1 + \delta)] = 0.01$.

Table 7. Volume filling factors of enriched gas in per centage derived from the two considered simulations: [a]Viel et al. (2013) and [b]Bolton & Becker (2009). The overdensity range corresponding to the inspected column densities is computed at the redshift of the simulations, $z = 2.8$. We define $M \equiv \log Z/Z_{\odot}$.

$\log N_{\mathrm{HI}}$ $(\delta + 1)$	[13.5 : 14.0] [1.3 : 3.1]	[14.0 : 14.8] [3.1 : 11.8]	[13.5 : 14.8] [1.3 : 11.8]
Reference model[a]			
Tot. Vol.	$\sim$12.7	$\sim$4.7	$\sim$17.4
$M \gtrsim -3$	$\sim$7.6	$\sim$2.8	$\sim$10.4
$M < -3$	$\sim$5.1	$\sim$1.9	$\sim$7.0
High-resolution model[b]			
Tot. Vol.	$\sim$10.1	$\sim$3.0	$\sim$13.1
$M \gtrsim -3$	$\sim$6.1	$\sim$1.8	$\sim$7.9
$M < -3$	$\sim$4.0	$\sim$1.2	$\sim$5.2

the volume enriched above a metallicity $\log Z/Z_{\odot} \sim -3$ becomes $\sim$10.4 per cent. A conservative upper limit to the enriched volume is determined from our limits on O VI: a maximum of 76 per cent of the gas with overdensities between $(\delta + 1) \simeq 1.3$ and 3.1 (corresponding to the column density range $13.5 \leq \log N_{\mathrm{HI}} < 14.0$ at $z = 2.8$) is enriched to $\log Z/Z_{\odot} \gtrsim -3$. This corresponds to an enriched volume fraction of $\sim$9.6 per cent which gives an upper limit of $\sim$12.5 per cent adding the contribution of the larger overdensities.

The higher resolution simulation predicts a smaller volume occupation for the range of overdensities considered in this work. In particular, for the column density range $14.0 \leq \log N_{\mathrm{HI}} < 14.8$ the occupied volume at $z = 2.8$ is 3.0 per cent, for the range $13.5 \leq \log N_{\mathrm{HI}} < 14.0$ is $\sim$10.1 per cent. These numbers translate into a maximum volume enriched to $\log Z/Z_{\odot} \gtrsim -3$ of $\sim$9.5 per cent. All the volume filling factors are detailed in Table 7.

It is relevant to note that the contribution of the regions traced by H I column densities $\log N_{\mathrm{HI}} > 14.8$ is negligible in terms of enriched volume as can be seen in Fig. 12.

5.3 Dependence on redshift

The association of H I lines with metal lines is a fundamental step which allows us to estimate the metallicity of the gas at different overdensities which, however, is always affected by a certain degree of uncertainty. If, for example, the metals are transported in the IGM by small metal-rich clumps that then lose their identity in H I, as suggested by Schaye, Carswell & Kim-S. (2007), many of the metallicities we are deriving could be considered only as average values and the real picture would be much more complicated.

With the aim of verifying if the results plotted in Figs 10 and 11 are reliable, we have considered only those absorbers for which we had either a detection or an upper limit for both C IV and O VI, disregarding the information on H I. Then, we have also investigated the possible effects of redshift, dividing the obtained sample in two redshift bins: $2.4902 \lesssim z < 2.758$ and $2.758 \lesssim z < 3.0255$.

The results are shown in Fig. 13, where the two redshift subsamples are compared with the predictions of the CLOUDY models described before, computed at the average redshifts of the subsamples, $z = 2.6$ and $z = 2.9$, respectively. The black, dashed lines mark the regions between $\log N_{\mathrm{HI}} = 14$ and 14.8 (see Fig. 10), and the column densities have been translated into overdensity values as already described in the previous section.

There is no evidence of a significant difference in the metallicity of the investigated gas in the two considered redshift bins.
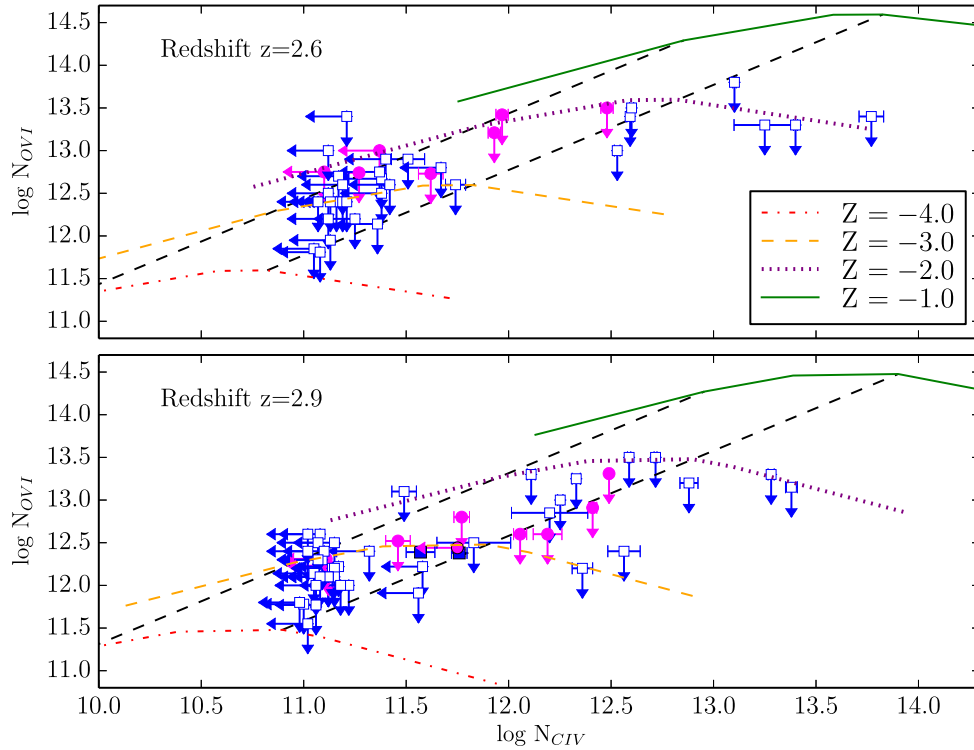
Figure 13. Absorption systems in our sample for which we have either an upper limit or a detection for C IV and O VI divided into two redshift bins: $2.4902 \lesssim z < 2.758$ (upper panel) and $2.758 \lesssim z < 3.0255$ (lower panel). Systems for which one or both values are upper limits are plotted as open symbols. Filled dots mark those systems for which C IV is a detection and O VI is a possible detection (only one of the line of the doublet is detected), while filled squares mark systems for which both C IV and O VI are detections (which for the O VI means that both lines of the doublet were detected). The superposed lines in the two plots are the predictions of the CLOUDY models described in Section 5 for the four metallicities listed in the caption, computed at the average redshift of the samples, $z = 2.6$ (upper panel) and $z = 2.9$ (lower panel). The black dashed lines join the model predictions for the four metallicities at $(\delta + 1) = 3.7$ and 14.1 at $z = 2.6$, and at $(\delta + 1) = 2.8$ and 10.8 at $z = 2.9$, corresponding to H I column densities of $\log N_{\rm HI} = 14$ and 14.8, respectively.

We confirm that in the overdensity regime where our observations are most sensitive, from $(\delta + 1) \simeq 2.8 - 3.7$ to $(\delta + 1) \simeq 10.8 - 14.1$, most of our measures indicate a metallicity $-3 \lesssim Z \lesssim -2$. In particular, the only two systems for which we have detected both C IV and O VI are at an overdensity of ∼5–10 and at a metallicity $Z \sim -3$. Considering the total sample (88 absorbers), we find that ∼40 per cent of the systems have a metallicity $Z < -3$. This percentage should be considered as a lower limit and would likely increase with the increase of the O VI statistics and of the SNR of the spectra.

6 CONCLUSIONS

In this work, we presented the analysis of the ultra-high SNR, high resolution spectrum (dubbed the *deep* spectrum) of the quasar HE0940-1050 ($z_{\rm em} = 3.0932$) obtained with the UVES spectrograph at the ESO VLT telescope. The aim of this observation was to shed light on the abundance and distribution of metals in the low density intergalactic gas at $z \sim 3$ in order to investigate the details of the enrichment process.

The investigated redshift range, $2.4902 \lesssim z \lesssim 3.0255$, was chosen in order to have at least the transitions Lyα and Lyβ of the H I Lyman series to allow a reliable determination of $N_{\rm HI}$. In this whole redshift interval the deep spectrum is sensitive at 3σ to C IV $\lambda 1548$ Å lines with column densities down to $\log N_{\rm CIV} \simeq 11.4$ (assuming a Doppler value $b = 7$ km s^{-1}), in 90 per cent of this interval the spectrum is sensitive to C IV lines down to $\log N_{\rm CIV} \simeq 11.3$ and in 60 per cent down to $\simeq 11.1$.

We searched also for O VI in same redshift interval. The search for weak O VI lines at $z \sim 3$ is hindered by the crowded Lyα and Lyβ forests. Indeed, we could detect (i.e. both lines of doublet were observed) only three weak O VI absorbers, of which two were identified independently of their association with a C IV absorber.

The observational data were then compared with the results of a grid of CLOUDY models obtained assuming solar chemical composition and varying the metallicity, the overdensity and the temperature of the slab of gas (see Section 5).

The main conclusions that can be drawn from our study are the following.

(1) All H I lines in our sample with column density $\log N_{\rm HI} \geq 14.8$ show an associated C IV absorption. In the range $14.0 \leq \log N_{\rm HI} < 14.8$, 43 per cent of H I lines has an associated C IV absorption with column density down to our sensitivity limit. At column densities $\log N_{\rm HI} < 14.0$, the detection rates drop to less than 10 per cent. The comparison with the outcome of our grid of CLOUDY models shows that even if the gas traced by these H I column densities was as enriched as the one at larger column densities, our spectrum would not have the sensitivity to probe it.

(2) The fraction of H I lines with $\log N_{\rm HI} \geq 14$ showing associated C IV detections in our sample is at least a factor of 2 larger than the fraction of H I lines in the same column density range, tracing the CGM of relatively bright Lyman break galaxies hosted by dark matter haloes of average mass $\sim 10^{12}$ M$_\odot$, as found by Rudie et al. ([2012](#), see Fig. [9](#)). This result suggests that metals could lie also at larger distances than 300 physical kpc from the considered galaxies

but also that they could be present around lower mass galaxies, in agreement with a variety of theoretical studies (Madau et al. e.g. 2001; Scannapieco, Madau & Ferrara 2002; Samui, Subramanian & Srianand 2008; Oppenheimer, Davé & Finlator 2009; Booth et al. 2012).

(3) In the range of overdensities in which our C IV data are most sensitive to low metallicities, from $(\delta + 1) \simeq 3.1$ to $(\delta + 1) \simeq 11.8$ (corresponding to the range of column densities $14 \leq \log N_{\mathrm{HI}} < 14.8$ at $z = 2.8$), the comparison with our grid of CLOUDY models indicates that between $\sim$38 and 60 per cent of the absorbers are enriched to metallicities $-3 \lesssim \log Z/Z_\odot \lesssim -1$, while the remaining $\sim$40–62 per cent have a metallicity lower than -3 (see Figs 10 and 11).

(4) Through a comparison with the predictions of two cosmological simulations, we derived that the volume filling factor of the IGM gas (down to the mean density) enriched to a metallicity $\log Z/Z_\odot \gtrsim -3$ should be of the order of $\sim$10–13 per cent. This is again in agreement with predictions by theoretical studies in which the IGM was enriched at high redshift by low mass objects.

As a final statement, we would like to underline that the main weakness of this study is that it is based on a single high-resolution quasar spectrum albeit with an exceedingly high signal-to-noise ratio.[6] Such amazing data are the result of a gigantic observational effort performed with the UVES spectrograph at the VLT, which will unlikely be repeatable on a short time-scale. As a consequence it will be difficult to have soon a significative sample of exceptional spectra as this one.

In the near future, the ESPRESSO spectrograph (Pepe et al. 2014), a second generation VLT instrument whose first light is expected in 2017, will provide an opportunity for further high SNR studies of quasars. It will offer the unique possibility of working at a resolution $R \sim 60\,000$ collecting the light from all four VLT telescopes at the same time, mimicking the outcome of a 16m-equivalent telescope. For the real breakthrough in this research field, however, we will have to wait 10-15 yr until the next generation of high-resolution spectrographs working on 30m-class telescopes will be on stage.

---

[6] The SNR per resolution element varies between $\sim$200 and 500 in the C IV forest at $2.4902 \lesssim z \lesssim 3.0255$, being larger than $\sim$350 in more than 80 per cent of the redshift interval.

REFERENCES

Adelberger K. L., Shapley A. E., Steidel C. C., Pettini M., Erb D. K., Reddy N. A., 2005, ApJ, 629, 636

Aguirre A., Hernquist L., Schaye J., Weinberg D. H., Katz N., Gardner J., 2001, ApJ, 560, 599

Aracil B., Petitjean P., Pichon C., Bergeron J., 2004, A&A, 419, 811

Ballester P., Modigliani A., Boitquin O., Cristiani S., Hanuschik R., Kaufer A., Wolf S., 2000, The Messenger, 101, 31

Barai P. et al., 2013, MNRAS, 430, 3213

Becker G. D., Bolton J. S., Haehnelt M. G., Sargent W. L. W., 2011, MNRAS, 410, 1096

Bergeron J., Aracil B., Petitjean P., Pichon C., 2002, A&A, 396, L11

Bergeron J. et al., 2004, The Messenger, 118, 40

Bertone S., Stoehr F., White S. D. M., 2005, MNRAS, 359, 1201

Boksenberg A., Sargent W. L. W., 2015, ApJS, 218, 7

Bolton J. S., Becker G. D., 2009, MNRAS, 398, 1

Booth et al., 2012, MNRAS, 420, 1053

Bordoloi R. et al., 2014, ApJ, 796, 136

Calura F., Matteucci F., 2006, MNRAS, 369, 465

Carswell R. F., Webb J. K., 2014, Astrophysics Source Code Library, record ascl:1408.015

Carswell B., Schaye J., Kim T-S., 2002, ApJ, 578, 43

Carswell R. F., Webb J. K., Cooke A. J., Irwin M. J., 2014, Astrophysics Source Code Library, record ascl:1408.017

Cen R., Chisari N. E., 2011, ApJ, 731, 11

Cen R., Miralda-Escudé J., Ostriker J. P., Rauch M., 1994, ApJ, 437, L9

Cicone C. et al., 2014, A&A, 562, 21

Cole S., Lacey C. G., Baugh C. M., Frenk C. S., 2000, MNRAS, 319, 168

Cowie L. L., Songaila A., 1998, Nature, 394, 44

Cowie L. L., Songaila A., Kim T.-S., Hu E. M., 1995, AJ, 109, 1522

Cupani G. et al., 2015a, Mem. Soc. Astron. Ital., 86, 502

Cupani G. et al., 2015b, in Taylor A. R., Rosolowsky E., eds, ASP Conf. Ser. Vol. 495, Astronomical Data Analysis Software and Systems XXIV. Astron. Soc. Pac., San Francisco, p. 289

D'Odorico V., Bruscoli M., Saitta F., Fontanot F., Viel M., Cristiani S., Monaco P., 2008, MNRAS, 389, 1727

D'Odorico V., Calura F., Cristiani S., Viel M., 2010, MNRAS, 401, 2715

Dekker H., D'Odorico S., Kaufer A., Delabre B., Kotzlowski H., 2000, Proc. SPIE, 4008, 534

Ellison S. L., Lewis G. F., Pettini M., Chaffee F. H., Irwin M. J., 1999, ApJ, 520, 456

Ellison S. L., Songaila A., Schaye J., Pettini M., 2000, AJ, 120, 1175

Ferland G. J. et al., 2013, Rev. Mex. Astron. Astrofis., 49, 137

Feruglio C., Maiolino R., Piconcelli E., Menci N., Aussel H., Lamastra A., Fiore F., 2010, A&A, 518L, 155

Fontana A., Ballester P., 1995, The Messenger, 80, 37

edsGonzaga S., Hack W., Fruchter A., Mack J. 2012, The DrizzlePac Handbook. STScI, Baltimore

Greene J. E., Zakamska N. L., Smith P. S., 2012, ApJ, 746, 86

Haardt F., Madau P., 2001 in Neumann D. M., Van J. T. T., eds, Clusters of Galaxies and the High Resdhift Universe Observed in X-rays: Recent Results of XMM-Newton and Chandra.

Harrison C. M., Alexander D. M., Mullaney J. R., Swinbank A. M., 2014, MNRAS, 441, 3306

Herbert-Fort S. Prochaska J. X., Dessauges-Zavadsky M., Ellison S. L., Howk J. C., Wolfe A. M., Prochter G. E., 2006, PASP, 118, 1077

Hui L., Gnedin N. Y., 1997, MNRAS, 292, 27

Katz N., Weinberg D. H., Hernquist L., 1996, ApJS, 105, 19

Kereš D., Katz N., Davé R., Fardal M., Weinberg D. H., 2009, MNRAS, 396, 2332

Liang C. J., Chen H.-W., 2014, MNRAS, 445, 2061

Lu L., Sargent W. L. W., Barlow T. A., Rauch M., 1998, preprint (astro-ph/9802189)

Madau P., Ferrara A., Rees M. J., 2001, ApJ, 555, 92

Maiolino R. et al., 2012, MNRAS, 425L, 66

Martin C. L., 2005, ApJ, 621, 227

Martin C. L., Scannapieco E., Ellison S. L., Hennawi J. F., Djorgovski S. G., Fournier A. P., 2010, ApJ, 721, 174

Misawa T., Charlton J. C., Eracleous M., 2014, ApJ, 792, 77

Molaro P. et al., 2013, A&A, 555, 68

Oppenheimer B. D., Davé R., Finlator K., 2009, MNRAS, 396, 729

Pepe F. et al., 2014, Astron. Nachr., 335, 8

Petitjean P., Mueket J. P., Kates R. E., 1995, A&A, 295, L9

Pettini M., Shapley A. E., Steidel C. C., Cuby J-G., Dickinson M., Moorwood A. F. M., Adelberger K. L., Giavalisco M., 2001, ApJ, 554, 981

Pieri M. M., Schaye J., Aguirre A., 2006, ApJ, 638, 45

Porciani C., Madau P., 2005, ApJ, 625, L43

Prochaska J. X., Weiner B., Chen H.-W., Mulchaey J., Cooksey K., 2011, ApJ, 740, 91

Rauch M., 1998, ARA&A, 36, 267

Rorai A. et al., 2016, MNRAS, in press

Rudie G. C. et al., 2012, ApJ, 750, 67

Rupke D. S., Veilleux S., 2011, ApJ, 729L, 27

Rupke D. S., Veilleux S., Sanders D. B., 2005, ApJS, 160, 115

Samui S., Subramaniana K., Srianand R., 2008, MNRAS, 385, 783

Scannapieco E., Ferrara A., Madau P., 2002, ApJ, 574, 590

Scannapieco E., Pichon C., Aracil B., Petitjean P., Thacker R. J., Pogosyan D., Bergeron J., Couchman H. M. P., 2006, MNRAS, 365, 615

Schaye J., 2001, ApJ, 559, 507

Schaye J., Aguirre A., Kim T-S., Theuns T., Rauch M., Sargent W. L. W., 2003, ApJ, 596, 768 (S03)

Schaye J., Carswell R. F., Kim T.-S., 2007, MNRAS, 379, 1169

Shapley A. E., Steidel C. C., Pettini M., Adelberger K. L., 2003, ApJ, 588, 65

Shen S., Madau P., Guedes J., Mayer L, Prochaska J. X., Wadsley J., 2013, ApJ 765, 89

Simcoe R. A., Sargent W. L. W., Rauch M., 2004, ApJ, 606, 92

Somerville R. S., Primack J. R., 1999, MNRAS, 310, 1087

Songaila A., Cowie L. L., 1996, AJ, 112, 335

Springel V., 2005, MNRAS, 364, 5

Springel V., Hernquist L., 2003, MNRAS, 339, 289

Steidel C. C., Erb D. K., Shapley A. E., Pettini M., Reddy N., Bogosavljević M., Rudie G. C., Rakic O., 2010, ApJ, 717, 289

Sturm E. et al., 2011, ApJ, 733L, 16

Tescari E., Viel M., D'Odorico V., Cristiani S., Calura F., Borgani S., Tornatore L., 2011, MNRAS, 411, 826

Tremonti C. A., Moustakas J., Diamond-Stanic A. M., 2007, ApJ, 663L, 77

Tumlinson J. et al., 2011, Science, 334, 948

Turner M. L., Schaye J., Steidel C. C., Rudie G. C., Strom A. L., 2014, MNRAS, 445, 794

Tytler D., 1987, ApJ, 321, 49

Tytler D., Fan X.-M., Burles S., Cottrell L., Davis C., Kirkman D., Zuo L., 1995, in Meylan G., ed., QSO Absorption Lines. Springer-Verlag, New York, p. 289

Vanzella E. et al., 2010, A&A, 513, 20

Veilleux S., Cecil G., Bland-Hawthorn J., 2005, ARA&A, 43, 769

Viel M., Becker G. D., Bolton J. S., Haehnelt M. G., 2013, Phys. Rev. D, 88, 043502

Weinberg D. et al., 1999, in Banday A. J., Sheth R. K., da Costa L. N., eds, Proc. MPA-ESO Cosmology Conf., Evolution of Large Scale Structure: From Recombination to Garching. Garching, Germany, p. 346

Weiner B. J. et al., 2009, ApJ, 692, 187

Werk J. K., Prochaska J. X., Thom C., Tumlinson J., Tripp T. M., O'Meara J. M., Peeples M. S., 2013, ApJ, 204, 17

APPENDIX A: PLOTS OF POSSIBLE O VI DETECTIONS
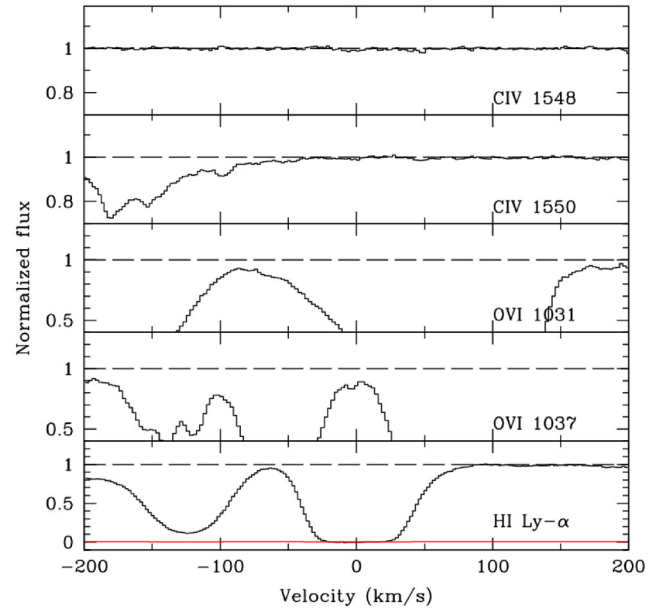
Figure A1. Possible detection of the transition O VI λ 1038 at $z_{abs} = 2.507\,588$ corresponding to $v = 0\,\mathrm{km\,s^{-1}}$ in the plot. C IV is not detected at this redshift.
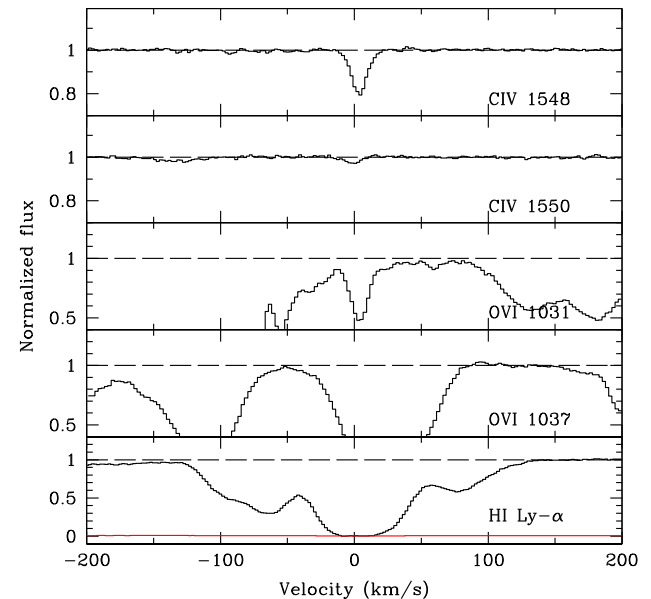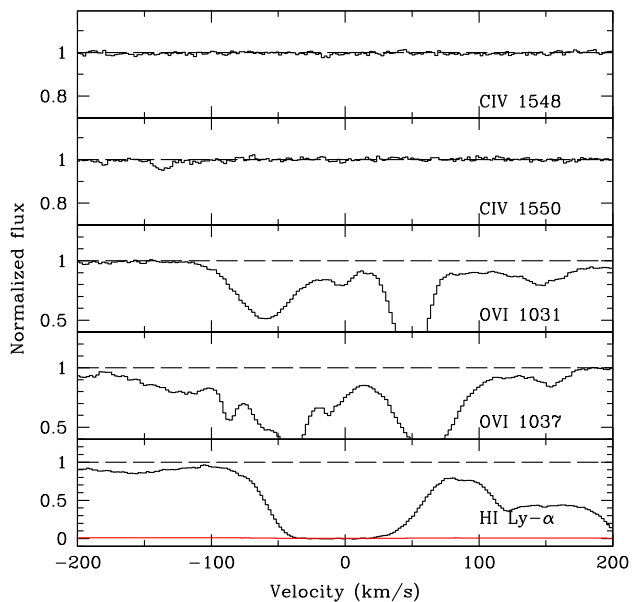

Figure A2. Detection of the C IV doublet (the transition at λ 1548 is blended) and possible detection of the transition O VI λ 1032 at $z_{abs} = 2.566\,402$.
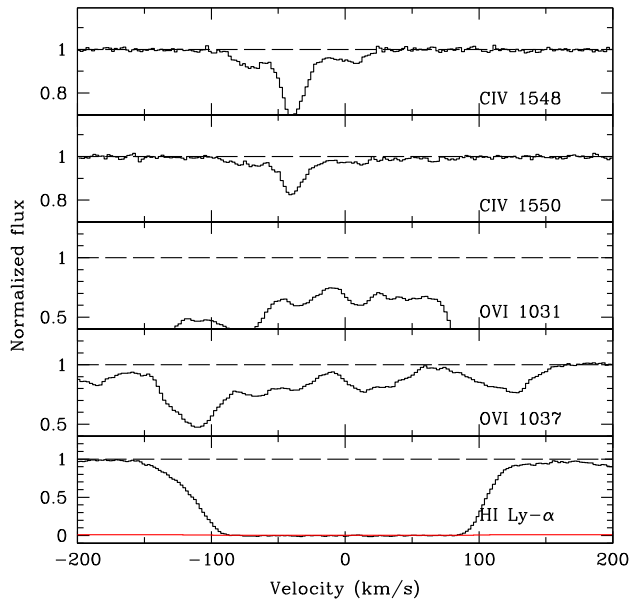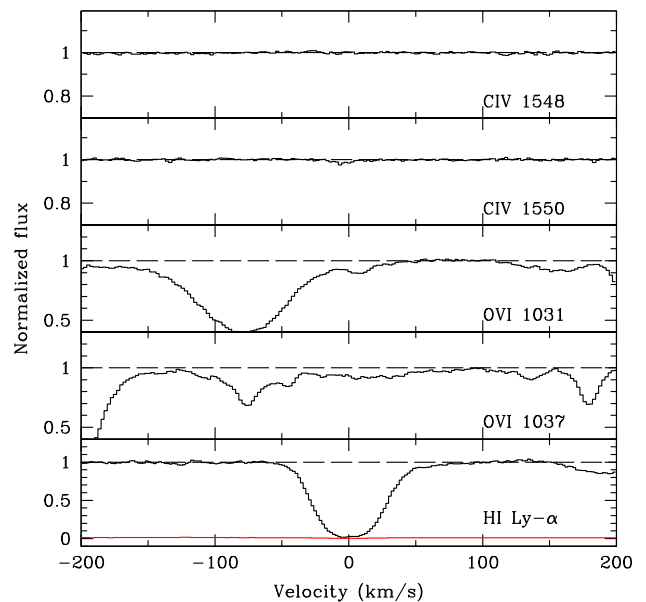
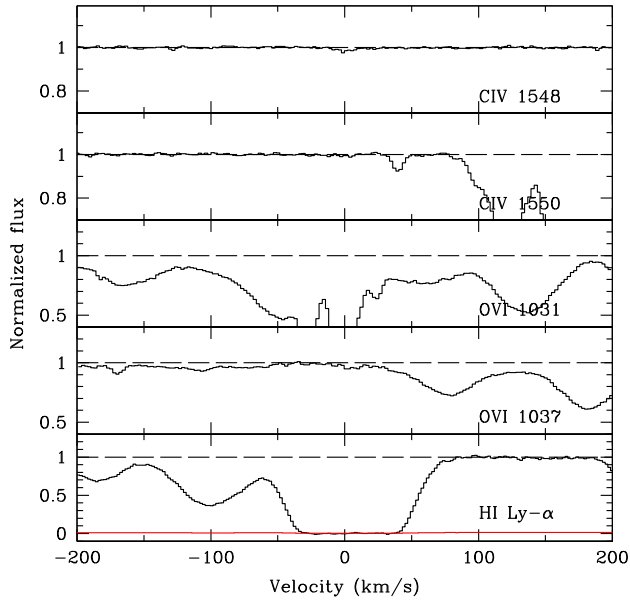**Figure A3.** Detection of the C IV doublet and possible detection of the transition O VI λ 1032 at z_{abs} = 2.643 643.
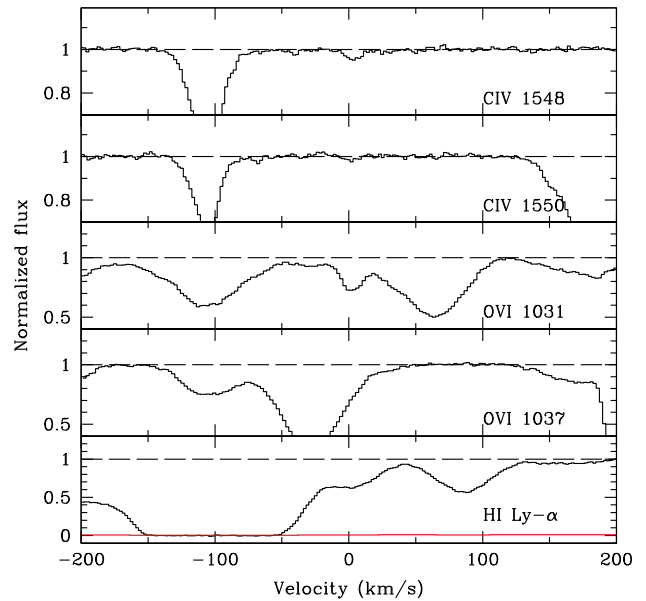
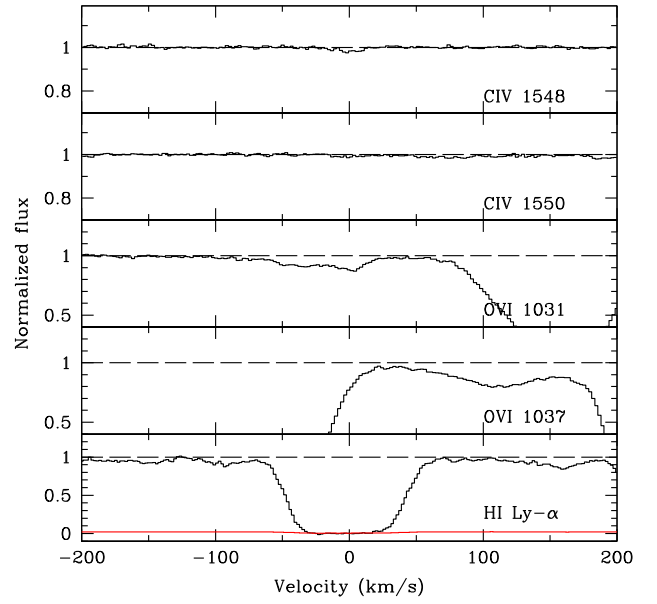**Figure A5.** Detection of the C IV doublet and possible detection of the transition O VI λ 1032 at z_{abs} = 2.659 215.

Figure A4. Possible detection of the transition O VI λ 1032 at z_{abs} = 2.654 839. C IV is not detected at this redshift.
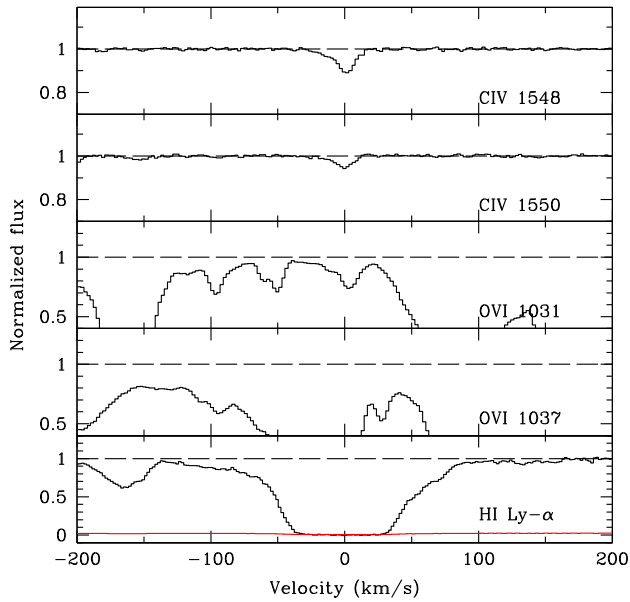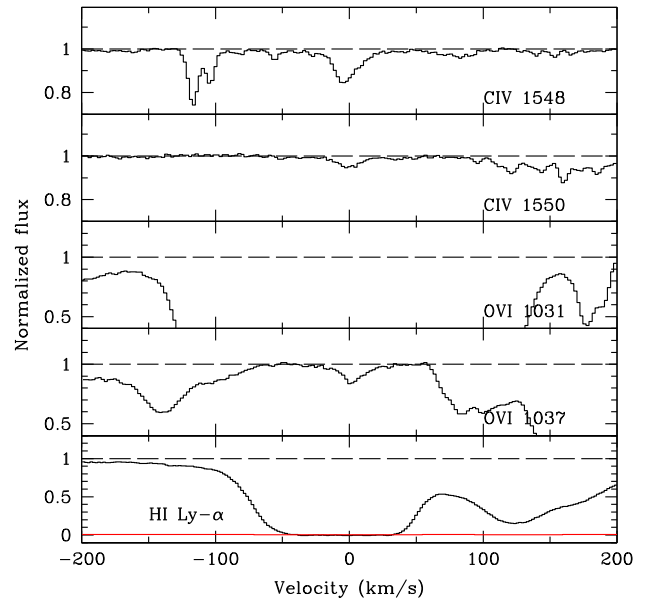

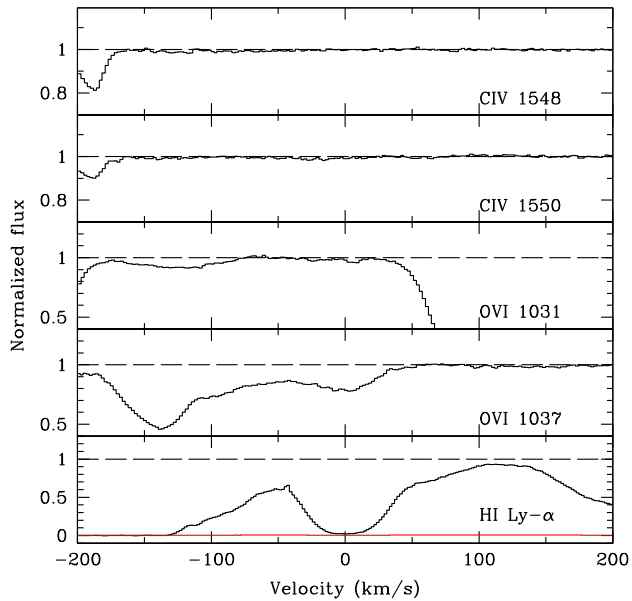**Figure A6.** Possible detection of the transition O VI λ 1032 at z_{abs} = 2.705 568. C IV is not detected at this redshift.

Figure A7. Detection of the weak C IV transition λ 1548 and possible detection of the transition O VI λ 1032 at $z_{abs} = 2.711\,67$.

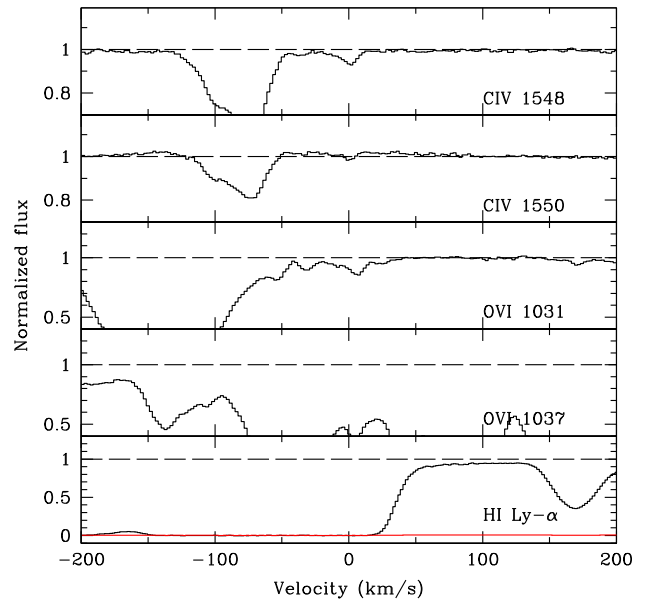**Figure A9.** Detection of the weak C IV transition λ 1548 and possible detection of the transition O VI λ 1032 at $z_{abs} = 2.785\,936$.

Figure A8. Detection of the C IV doublet and possible detection of the transition O VI λ 1032 at $z_{abs} = 2.771\,388$.
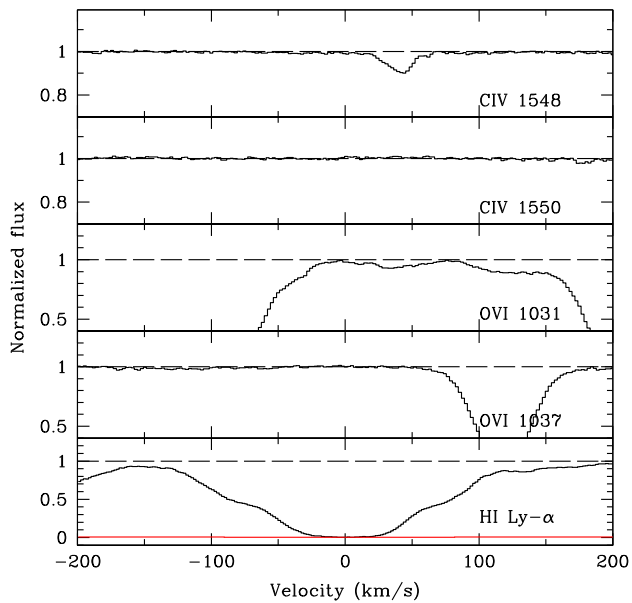
Figure A10. Detection of the C IV doublet and possible detection of the transition O VI λ 1038 at $z_{abs} = 2.810\,878$.
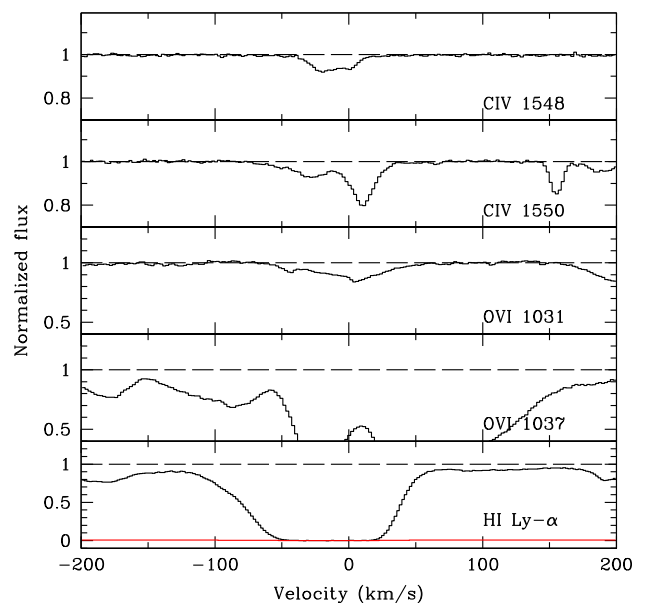
Figure A11. Possible detection of the transition O VI λ 1032 at z_{abs} = 2.863 317. C IV is not detected at this redshift.

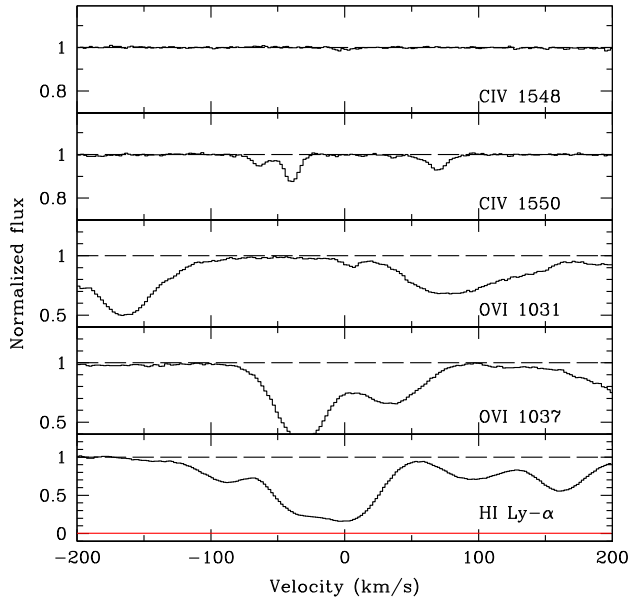**Figure A12.** Possible detection of the transition O VI λ 1032 at z_{abs} = 2.566 402. C IV is not detected at this redshift.

Figure A13. Detection of the C IV doublet and possible detection of the transition O VI λ 1032 at z_{abs} = 2.918 023.

Figure A14. Detection of the C IV doublet (the transition λ 1551 is blended) and possible detection of the transition O VI λ 1032 at z_{abs} = 2.931 062.

Figure A15. Detection of the weak C IV transition λ 1548 and possible detection of the transition O VI λ 1032 at $z_{abs} = 2.982\,51$.

This paper has been typeset from a TEX/LATEX file prepared by the author.